



Full Length Article

A hybrid computational approach for modeling cold spray deposition



Abba A. Abubakar ^{a,b}

^a Mechanical Engineering Department, King Fahd University of Petroleum and Minerals, Dhahran, 31261, Saudi Arabia

^b Interdisciplinary Research Center for Advanced Materials (IRC-AM), King Fahd University of Petroleum and Minerals, Dhahran, 31261, Saudi Arabia

ARTICLE INFO

Keywords:

Cold spray deposition
Coating layer
Wear resistance
Point cloud
Finite elements

ABSTRACT

Cold spray (CS) is a cold-state technology that uses high-velocity supersonic gas flow to propel and deposit powder particles onto a substrate surface. The design and optimization of the cold spray deposition process were recently achieved via the experimental trial-and-error approach, which is laborious and costly. The present study presents a computationally efficient hybrid method for simulating cold spray coating deposition, applied explicitly to Ni coating used for wear applications. The model effectively synergizes meshless and meshed computational schemes in predicting the thermo-mechanical deformation of the impacting Ni particles and SS304 steel substrate. During the simulations, the point cloud (PC) of deformed particle domains is converted into a high-quality finite element (FE) mesh with novel PC processing algorithms. The simulations are carried out for various particle characteristics and spraying conditions. The numerical predictions are validated by comparing them with other numerical schemes and previous experimental studies. The main results indicate that the kinetic energy and morphology of the impacting Ni particles strongly influence plastic deformation and temperature rise in the substrate and predeposited coating particles. Plastic deformation is more prominent at the particle edges and mating material interfaces. At the same time, the temperature rise does not reach the melting point but can allow for recrystallization near highly localized regions of the coating microstructure, even at lower deposition rates. Compressive residual stresses are also observed across the coating and substrate layers, with a non-uniform and nonlinear residual stress field due to complex interactions among neighboring particles. The study aims to provide a robust numerical framework for designing and optimizing cold spray deposition parameters for industrial coatings, bridging the knowledge gap and enabling efficient and cost-effective simulations for process optimization.

1. Introduction

High-velocity gas flow is used in the cold spray (CS) process to deposit powdered particles onto the substrate surface while they are still in the solid state [1]. Due to the metallurgical bonding and mechanical interlocking produced by plastic deformation and heat dissipation [2], the propelled particles adhere to the substrate upon impact. The CS process is appropriate for depositing metallic coatings, prototyping, or repairing cracked components since it does not involve particle melting, solidification, or phase transformations, nor does it induce high tensile residual stresses in the deposited structures [2–4]. Moreover, using CS for metalizing polymers is becoming increasingly popular [5,6]. Even though CS research has advanced significantly, CS deposition simulation work is still in its early stages. When dealing with several particles with different characteristics, the numerical simulation of particle impact and deformation produces extremely nonlinear events that are computationally difficult to solve. Recently, various numerical schemes, such as

Lagrangian [7], Eulerian [8], Combined-Eulerian-Lagrangian (CEL) [9], or Arbitrary-Lagrangian-Eulerian (ALE) [10] have been used to model the CS process using the finite element method. In addition, smooth particle hydrodynamics (SPH) is used to model the CS process [11]. By employing proper time-integration methods and acceptable boundary conditions, these numerical schemes, as opposed to experiments, can quantitatively predict the particle–substrate deformation for any given set of CS parameters. As a result, numerical simulations could reduce the time and money spent on the repeated (trial-and-error) tests required to optimize the key CS parameters (such as powder particle characteristics, nozzle geometry, stand-off distance, spray angle, gas flow rate, powder feed rate, scan speed, etc.) that affects the effective properties of the coating layer. See (Table 1).

Several research works [9,10] have focused on conducting parametric studies through numerical simulation to investigate the influence of key CS parameters on the evolution of deposit layer thickness, porosity, temperature, and residual stresses. To reduce the high cost and

E-mail address: abba.abubakar@kfupm.edu.sa.

<https://doi.org/10.1016/j.jestch.2023.101579>

Received 9 January 2023; Received in revised form 23 July 2023; Accepted 1 November 2023

Available online 16 November 2023

2215-0986/© 2023 Karabuk University. Publishing services by Elsevier B.V. This is an open access article under the CC BY-NC-ND license (<http://creativecommons.org/licenses/by-nc-nd/4.0/>).

Table 1

Material parameters used in the simulations as obtained from Ref. [30].

Parameter	Material Type	Ni	Ti	SS304
$\rho(\text{kg/m}^3)$		8906	4510	7920
$k(\text{W/mK})$		91/300 K 71/1073 K	11.4/300 K 16/1073 K	16.2/300 K 26.0/1073 K
$C_p(\text{J/kgK})$		456/300 K 490/1073 K	528/300 K 615/1073 K	450/300 K 640/1073 K
$G(\text{GPa})$		76	30	86
$T_m(\text{K})$		1726	1923	1800
$C_0(\text{m/s})$		4542	5020	4570
Γ_0		1.83	1.23	1.93
s		1.5	1.53	1.49
$A(\text{MPa})$		163	807	260
$B(\text{MPa})$		648	482	1350
C		0.006	0.019	0.020
n		0.330	0.319	0.620
m		1.440	0.66	1.000

computing complexity of the numerical simulations, some researchers used two-dimensional (2D) axisymmetric [12] or symmetric three-dimensional (3D) models [7]. While full 3D models involving multiple particles are adopted in other works [9]. The Preston-Tonks-Wallace and Johnson-Cook material models are frequently used to simulate the deformation of the particle–substrate interface during metallic particle deposition [13,14]. The interacting forces between the particle and substrate domains are often defined using a combination of normal and sliding contact formulations [7,9,10,12]. However, a recent study suggests a superior formulation was established based on traction separation laws [15,16]. It is found that high accuracy Lagrangian finite element (FE) scheme could accurately predict the experimental rebound velocities and critical bonding conditions during the spraying of pure Cu onto Cu substrate [7]. The FE simulations revealed that about 99 % of particles kinetic energy is dissipated through plastic deformation [7]. Ti-6Al-4 V Grade 23 coating adhesion strength onto Ti-6Al-4 V Grade 5 substrate is also predicted using a Lagrangian FE approach using historical data on the nodal temperature at the particle–substrate interface from FE simulations. [17]. It has been shown that the particle temperature, then the particle impact speed, have the most effects on the adhesion strength of Ti-6Al-4 V Grade 23 coating [17]. A different study [12] uses the Lagrangian FE simulations to investigate the shot peening of Ti6Al4V particles deposited onto the Ti6Al4V substrate. The localized plastic deformation caused by the shot peening resulted in localized melting temperature of Ti6Al4V particles. The primary drawbacks of the Lagrangian FE scheme, which are not present in the Eulerian scheme [8], are the numerical challenges caused by severe mesh distortion during particle deformations [18]. On the other hand, the need for a fine mesh, which lengthens computation times, and the coalescence of material interfaces, which makes it challenging to distinguish the particle/substrate interfaces are some of the drawbacks of the Eulerian scheme [19]. The SPH technique works well with large deformation CS simulations since there is no element distortion issue. However, tensile instability, increased computational time for multi-particle domains, large memory utilization, and poor contact interactions due to pseudo-particles are the main drawbacks of SPH [19]. As a result, the ALE or CEL techniques are used in the majority of CS simulation studies. The ALE simulations were used to predict the temperature and residual stress distribution during the CS deposition of Cu, Al, and stainless steel [10,13,20]. It is shown that jetting out phenomenon is more pronounced during spraying soft metallic particles (such as Al and Cu) [10]. Additionally, the degree of particle jetting in Cu and stainless steel increases when the impact velocity and temperature rise. The particle materials, impact velocity, and temperature affect the temperature distribution and residual stress field in the coating layer [13,20]. The residual stress is found to be mainly compressive and equibiaxial, and its magnitude increases with increasing particle temperature, impacting velocity and

coating layer thickness for Cu coatings deposited onto Cu substrate [11]. Another study [21] uses an ALE simulation to examine how stand-off distance and scanning speed affect the temperature buildup in Ni coating deposited onto the Al substrate. It has been demonstrated that the temperature of the Ni coating layer rises as the stand-off distance and scanning speed decrease [21]. Although the element distortion issue in the Lagrangian scheme can be resolved using the ALE scheme, the ALE takes several simulation steps due to the necessity of continuous remeshing, which can greatly increase the computational time [19]. The accuracy of the simulation results achieved by the ALE technique is also impacted by interpolation errors, higher strain gradients and remeshing frequency, particularly near the particle boundaries [19]. CEL is the most robust and reliable numerical scheme among the earlier described methods [18,19]. The CEL scheme can seamlessly handle the impact deformation of multiple particles. Moreover, it predicts any jetting and excessive particle deformation without encountering element distortion or tensile instability problems [18,19]. The main drawbacks of this scheme are, however, the coalescence of the particle interface and the high computing cost resulting from the demand for a highly dense mesh across the entire space for particle motion and deformation [18,19]. A recent study [9] used CEL to design a solid freestanding porous structure. The simulation results demonstrate that compared to Al, utilizing Cu sacrificial powder particles resulted in better inter-particle bonding in Ti-based porous structures. Furthermore, strongly connected pore networks were produced within a specific range of the sacrificial powder volume fraction. To simulate the evolution of the coating layer during the deposition of Cu/Al unto Cu/Al substrates, a material addition/deletion technique involving simplified geometries is commonly used [22,23]. This is to avoid the computational complexities associated with the limitations of the FE-based schemes mentioned earlier [19]. A recent study shows that the hybrid computational approach, previously developed for droplets impact under thermal spray deposition (TSD), could be more effective and computationally efficient in simulating the CS process [19]. The hybrid approach leverages the advantages of both the meshless (i.e., SPH) and meshed (i.e., Lagrangian) numerical schemes by combining simulations on the point cloud (PC) and finite element (FE) as previously demonstrated for ZrO₂ onto stainless steel [24–26]. The hybrid approach is, therefore, more appropriate for the CS process because, unlike in TSD, CS deposition involves the impact and plastic deformation of solid particles. The hybrid scheme reduces the numerical difficulties caused by the severe element distortions, high computational intensity, tensile instability, and multi-particle interactions faced with some of the earlier methods.

The present study proposes using the physics-based hybrid scheme to model the CS deposition of metallic coatings. The hybrid approach synergizes simulation results obtained with the smooth particle hydrodynamics (SPH) and the finite element method (FEM). The impacting particle deformations are solved with the SPH formulations on point cloud (PC). In contrast, the substrate deformation and the previously deposited particles are predicted with the finite element (FE) grid. Data conversion and transfer from the PC to FE domains are achieved during the simulations via PC processing algorithms. The conversion/data transfer process is straightforward and computationally inexpensive. The approach is used to predict the mechanical deformation, temperature distribution, and residual stresses developed during the CS deposition of Ni coating onto stainless steel (SS304) substrate. In the energy industries [27], Ni coating is commonly used to provide wear and corrosion resistance to steel surfaces exposed to high temperatures; as a result, the hybrid scheme could be an appropriate choice for optimizing the CS parameters. The CS simulations are conducted for various ranges of particles and impact characteristics. The numerical simulation results are validated by comparing them with previous experiments and FE-based schemes. The study aims to set a robust numerical framework for effectively simulating the CS process for coating deposition.

2. Methodology

As the spray process involves multiple particles impacts and deformation, the local force balance and the energy equations (i.e., Eq. (1) and Eq. (2)) are solved to effectively predict the plastic deformation and heat dissipation caused by the high-velocity impact phenomenon.

$$\rho \frac{\partial^2 \bar{u}}{\partial t^2} = \nabla \bullet \tilde{\sigma} + \rho \bar{b} \quad (1)$$

Here: \bar{u} denotes displacement, $\tilde{\sigma}$ is the Cauchy stress, ρ is material density, \bar{b} is body force per unit mass, and t is time.

The Cauchy stress tensor ($\tilde{\sigma}$) relates to the total strain tensor ($\tilde{\varepsilon}$) via the Hooke's law:

$$\tilde{\sigma} = \tilde{C} : (\tilde{\varepsilon} - \tilde{\varepsilon}_{th} - \tilde{\varepsilon}_{pl}) \quad (2)$$

$$\tilde{\varepsilon} = \tilde{\varepsilon}_{el} + \tilde{\varepsilon}_{th} + \tilde{\varepsilon}_{pl} \quad (3)$$

Here: $\tilde{\varepsilon}_{el}$ denotes the elastic strain, $\tilde{\varepsilon}_{th}$ is the thermal strain, and $\tilde{\varepsilon}_{pl}$ is the plastic strain. During cold spraying [28], about 99 % of the impacting particles' kinetic energy is dissipated through plastic deformation and heat energies. The recoverable elastic strain is, therefore, negligibly small. Furthermore, even though thermal strain was

considered in the present study, it is not very significant because a metal-to-metal interface is being evaluated.

The particle and substrate deformations can be predicted from:

$$\tilde{\varepsilon} = \frac{1}{2} ((\nabla \bar{u})^T + \nabla \bar{u}) \quad (4)$$

The thermal strain can be predicted from:

$$\tilde{\varepsilon}_{th} = \int_{T_0}^T \alpha \bullet dT \quad (5)$$

The plastic flow rule for the evolution of plastic strain in the deforming bodies can be expressed as:

$$d\tilde{\varepsilon}_{pl} = d\lambda \bullet \frac{\partial Q}{\partial \tilde{\sigma}} = \frac{3}{2} d\lambda \bullet \frac{\tilde{S}}{\tilde{\sigma}_{eq}} \quad (6)$$

where: $d\tilde{\varepsilon}_{pl}$ is the plastic strain rate, $Q = \tilde{\sigma}_{eq} - \tilde{\sigma}_{yp}$ is the yield function, \tilde{S} is the deviatoric stress, $\tilde{\sigma}_{eq} = \sqrt{\frac{3}{2}\tilde{S} : \tilde{S}}$ is the von Mises stress, $\tilde{\sigma}_{yp}$ is yield strength, and $d\lambda$ is the plastic multiplier.

To incorporate the influence on thermal softening and loading rate, the Johnson-Cook material model is used to predict the evolution of equivalent plastic strain during particle and substrate deformations as commonly done [19]. With this model, the initial yield surface is

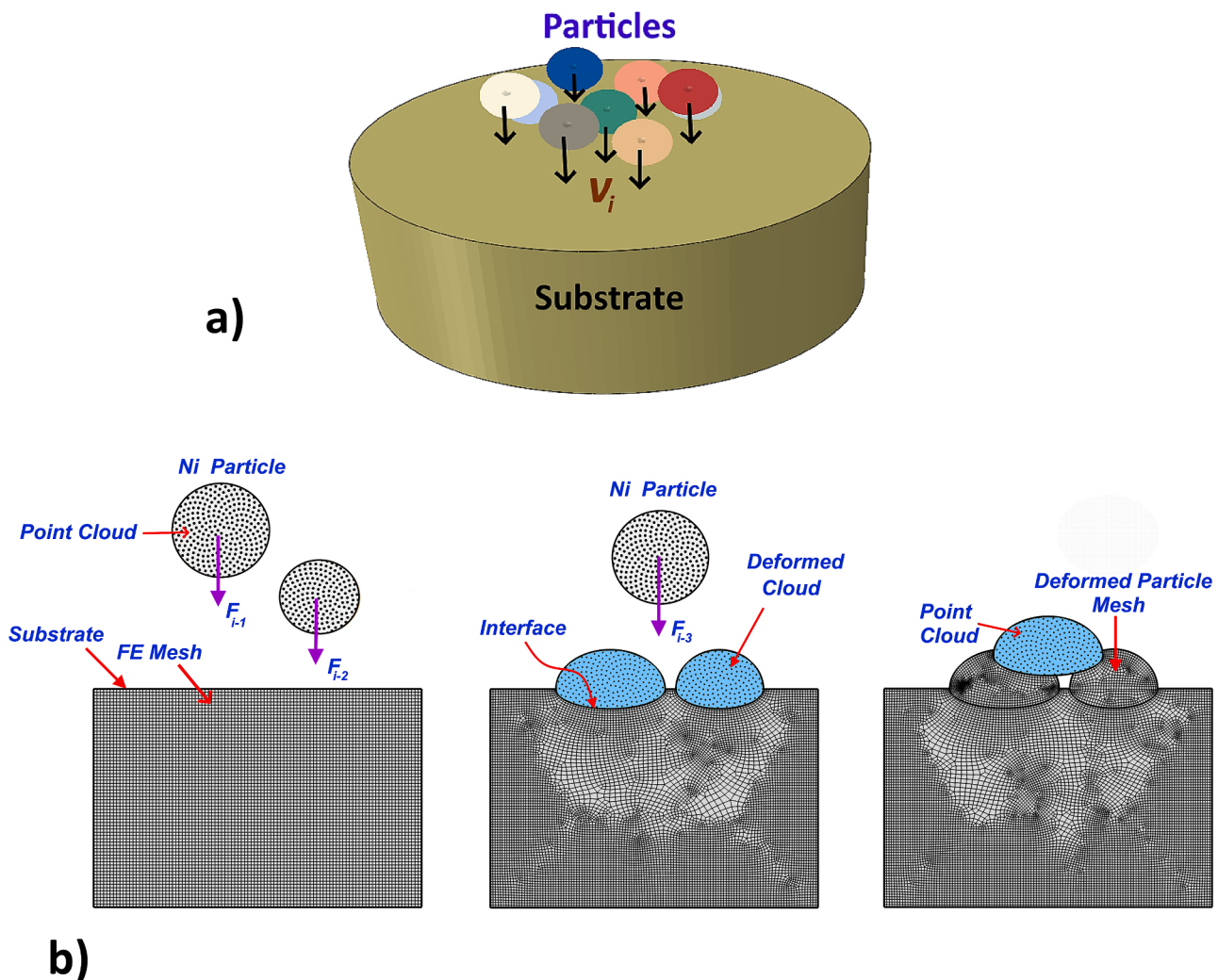


Fig. 1. Typical demonstration of the: a) deposition of multiple 25 μm Ni particles impacting on $\phi 200 \mu\text{m} \times 100 \mu\text{m}$ cylindrical substrate and b) hybrid computational approach. The substrate domain is discretized with Lagrangian finite element scheme, while the particle domains are discretized with the smooth particle hydro-dynamics scheme.

expressed as:

$$\tilde{\delta}_{yp} = [A + B(\epsilon_{pl})^n] \left[1 + C \ln \left(d \frac{\tilde{\epsilon}_{pl}}{d\tilde{\epsilon}_0} \right) \right] (1 - \hat{\theta}^m) \quad (7)$$

where: ϵ_{pl} denotes the equivalent plastic strain, $d\tilde{\epsilon}_{pl}$ is incremental plastic strain rate, $d\tilde{\epsilon}_0$ is the reference plastic strain rate, $\hat{\theta}$ is non-dimensional temperature, A, B, m, n are material parameters obtained from experimental stress-strain curves.

2.1. Initial conditions

Ni particles with varying impacting characteristics such as different sizes, shapes, impact velocities, and temperatures are propelled onto SS304 stainless steel substrate as demonstrated in Fig. 1a. A cylindrical substrate domain with the dimensions $\phi 100 \mu\text{m} \times 160 \mu\text{m}$ is used for the numerical simulations. The substrate dimensions are carefully selected through preliminary parametric analyses to reduce boundary effects on the outcomes of the numerical simulation as done in previous works [24,25]. The substrate domain is assumed to be initially at the ambient temperature (i.e., 300 K). The substrate is stationary, while the particles are pre-assigned initial velocities and temperatures. The particle temperatures and impact velocities are varied from 300 K to 600 K and 125 m/s – 1250 m/s according to spraying parameters given in Table S1. The single, double, and multiparticle impact of Ni powder particles with various morphologies or shapes, i.e., spherical, hollow spherical, oblate, rod-like, angular, and flake-like shapes, are simulated. The particle equivalent sizes range from 5 μm – 60 μm spherical particles. The spraying parameters in Table S1 are calculated based on the critical bonding condition for spraying with D42PBI nozzle and K8000-92 HSU equipment (CGT cold gas technology GmbH, Ampfing, Germany) as provided by the web-based kinetic spray solution software (GTV Company, Buchholz, Germany) [29]. To effectively validate the simulation results, the deposition parameters in Table S1 are chosen to produce particle impact velocity and temperature that are within a similar range to that of a prior study by Nikbakht et al. [30], in which an average impact velocity of $483 \pm 70 \text{ m/s}$ and $459 \pm 61 \text{ m/s}$ was found for a 25 μm Ni particle and 30 μm Ti particle, respectively. The average impact temperature of 300 K was used for Ni and Ti particles in the previous study [30]. The particle impact locations are randomly located for the multiparticle layer simulations to conform with the typical interparticle interactions encountered during the cold spray (CS) process.

2.2. Boundary conditions

With the SPH technique, point cloud (PC) or particle domains implicitly interact with one another via the smoothing kernel function; thus, the simulations naturally reflect interactions among particle-particle interfaces [31]. Moreover, in the Abaqus/CAE package, the ghost particle method is used to define the contact interactions between the PC and meshed target surface [31]. As a result, the ghost particle method is used to determine the interfacial deformation or adhesion between the impacting particles and meshed target surface. In addition, the Abaqus/Explicit general contact algorithm is used to define the normal and tangential contact behavior at the particle-substrate interface, as suggested in earlier studies [32]. As previously done, the normal contact behavior is defined based on the hard contact formulation to capture the pressure-overclosure relationship with kinematic contact mechanical constraint [10]. At the same time, the tangential contact behavior at the interface is defined via the penalty formulation and a friction coefficient of 0.5 [10,30]. A finite sliding scheme was employed to allow a finite motion of the contact surfaces. The bottom face is constraint to move in all directions to prevent rigid body motion in the SS340 substrate. According to customary practice [10], the inelastic heat dissipation index in the particle and substrate domains is set at 0.9.

2.3. Numerical implementation

The smooth particle hydrodynamics (SPH) meshless approach is used to discretize the governing equations for plastic deformation and temperature evolution in the particle domains on the point cloud (PC) (Fig. 1). On the other hand, the governing equations for the plastic deformation of the substrate and predeposited coating (splat) structures are discretized on the mesh grid following the finite element method (FEM). Within the commercial FEA tool, ABAQUS/Explicit [31], the discretized equations are implemented in three dimensions (3D) on Lagrangian domains. Given the high spray rate and the highly dynamic nature of CS deposition, the explicit/dynamic method is more appropriate for simulating particle impact deformation, as pointed out in our previous study [26]. The simulations are conducted using temperature-dependent structural and thermal properties based on isotropic material behavior and Johnson-Cook (JC) plasticity model (Table 2) [30]. The material parameters for the powder and substrate materials are selected from a previous study in which the Lagrangian FE scheme is used to model the CS deposition using the JC model [30]. This model accounts for strain hardening, strain rate hardening, and thermal softening; thus, the work-hardening effect on previously deposited particles is inherently captured in the JC model [33,34]. The model is frequently calibrated using stress-strain relations obtained through single-particle compression experiments to predict the particles' deformation during cold spraying accurately. This becomes important when particles are subjected to excessively high strain rates or when suitable powder JC material parameters are unavailable [34]. The linear elastic response of the particles and substrate are effectively calibrated with the Mie-Grüneisen equation of state according to parameters provided in previous works [35]. The SPH model is solved with PC3D elements. In contrast, the FEM counterpart is solved with solid continuum (tetrahedral or hexahedral) elements, as shown in Fig. 1b. When the PC-based particles reach the points of maximum deformation during the simulations, they are transformed into high-quality FE mesh domains. As illustrated in Fig. 2, the in-house python code developed based on algorithms in the PyMeshLab framework is used to construct the PC processing algorithms required for the PC-to-FE conversion. The algorithms include: 3D alpha-shape, Poisson-disk sampling, Poisson surface reconstruction, quadratic-edge decimation, and least square subdivision surface algorithm. Further details about the implementation of the PC processing algorithms can be found in our previous research works dealing with thermal spray deposition [24–26]. Nodal coordinates of the deformed particles are extracted and fed into the 3D alpha-shape algorithm for reconstruction of the deformed 3D particles shape (with $\alpha = 2.5\%$ of bounding box diagonal). The Poisson-disk sampling algorithm is used to create 300 – 500 sample points using the parameters: *over-sampling rate* = 20 and *sampling pool size* = 10. The Poisson surface reconstruction algorithm is used to reconstruct the stereolithographic (STL) mesh of the deposited particles using point normal vectors of the 300 – 500 sample points and the parameters: *octree depth* = 9, *solver divide* = 8 and *sample per node* = 1. Quadratic-edge decimation and least square subdivision surface algorithms are used to refine the STL mesh where necessary with the appropriate number of triangular elements, element quality index, and refinement levels. The Tri-to-Tetra algorithm of Abaqus code

Table 2

Comparison of particle flattening ratio obtained with the proposed hybrid approach, ALE method and previous experimental observations [30].

Case	Size and Material of Particles	Flattening Ratio		
		Hybrid	ALE	Exp. [30]
A	Ni (25 μm)	0.56	0.49	0.52
B	Ti (30 μm)	0.23	0.20	0.37
C	Ni/Ti (30 μm /25 μm)	0.47/0.44	0.43/0.41	0.57/0.52
D	Ni/Ni/Ni (25 μm /22 μm /18 μm)	0.80/0.82/0.61	0.76/0.77/0.50	0.72/0.77/0.39

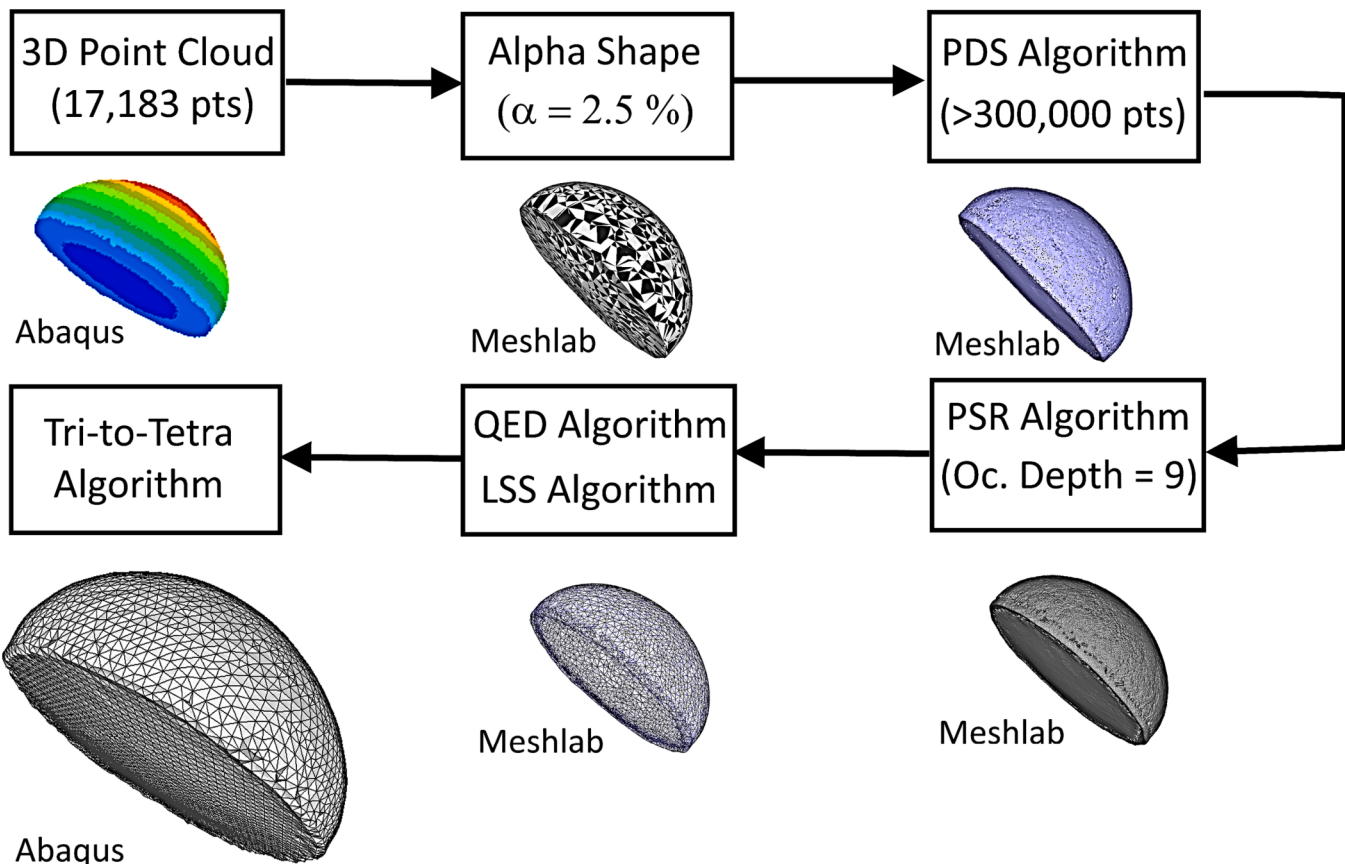


Fig. 2. Demonstration of conversion steps from point cloud into finite element mesh domains.

generates a high-quality FE mesh of deformed particle bodies from the STL mesh created with the point-cloud processing algorithms. The density of the PC and FE mesh is optimized via a series of grid-independent tests. Furthermore, the minimum time steps for obtaining stable solutions are determined with the help of the built-in (automatic) time-stepping algorithm of Abaqus/explicit. The variation of total kinetic and internal energies is tracked during simulations to ensure the consistency and stability of the numerical results obtained with an explicit time-stepping scheme. It is found that the total kinetic energy at the end of particle deformation is only a small fraction (less than 10 %) of the total internal energy; thus, this indicates a stable numerical simulation result. Additional details regarding convergence studies are also given in Appendix A (Fig. S1 - S5).

3. Results and discussion

The present study introduces a physics-based hybrid computational approach for modeling cold spray (CS) deposition. The hybrid approach couples simulation results obtained with the smooth particle hydrodynamics (SPH) and the Lagrangian finite element (FE) schemes to predict the thermo-mechanical deformation of cold sprayed Ni particles on SS304 steel substrate. The CS simulations are carried out for various particle characteristics and impact conditions. The numerical results are validated by comparing them with those obtained in previous experiments and FE-based simulations.

3.1. Validation of the hybrid computational model

This section aims to show how well the hybrid technique captures the dynamics of particle impact and deformation that occurs during the CS process. Ni particles were chosen for the current study because of the widespread usage of Ni coating in providing wear and corrosion

resistance to steel surfaces subjected to high temperatures [27,30]. The sequential impact of single and multiple spherical Ni/Ti particles is examined to assess the computational accuracy and effectiveness of the presented approach. The validation is expanded to include Ti particles to demonstrate the robustness of the hybrid approach in predicting inter-particle deformation occurring in the mixed material CS system. The simulation test cases involve various sizes of Ni and Ti particles, each consisting of at least 89,094-point sets in the form of a point cloud (PC). In line with the previous study by Nikbakht et al. [30], the initial impacting temperatures of the Ni/Ti particles are taken to be 300 K for all the cases. The varying size Ni/Ti particles have distinct initial impact velocities. To adequately compare the current simulation results with experimental findings, the initial impact velocities are chosen to be in a similar range to the previous study by Nikbakht et al. [30]. Moreover, the web-based kinetic spray solution program (GTV Company, Buchholz, Germany) is used to predict the initial impact velocities for the cases involving different Ni/Ti particle sizes [29]. Fig. 3 compares the impact deformation of single 25 μm Ni and 30 μm Ti particles as obtained with the current simulation approach and earlier experiments [30]. The Ni and Ti particles are assigned an initial impact velocity of 500 m/s in the numerical simulations as estimated using laser measurements in the previous study [30]. The double and triple impact cases are demonstrated in Fig. 4. In Fig. 4a and 4c, 25 μm Ti and 30 μm Ni particles impacting at 500 m/s are considered for the double impact cases. While for the triple impact cases shown in Fig. 4b and 4d, the sequential impact of 25 μm , 22 μm , and 18 μm Ni particles is considered. Different particle sizes are used because of statistical variation in powder particle sizes presented in the previous study [30]. As a result, the initial impact velocities for the three impacting particles are assumed to be slightly different in the simulation case presented in Fig. 4d. The initial impact velocities are estimated using the KKS software (Table S1). According to calculations in KKS software, a 25 μm Ni particle impacts the

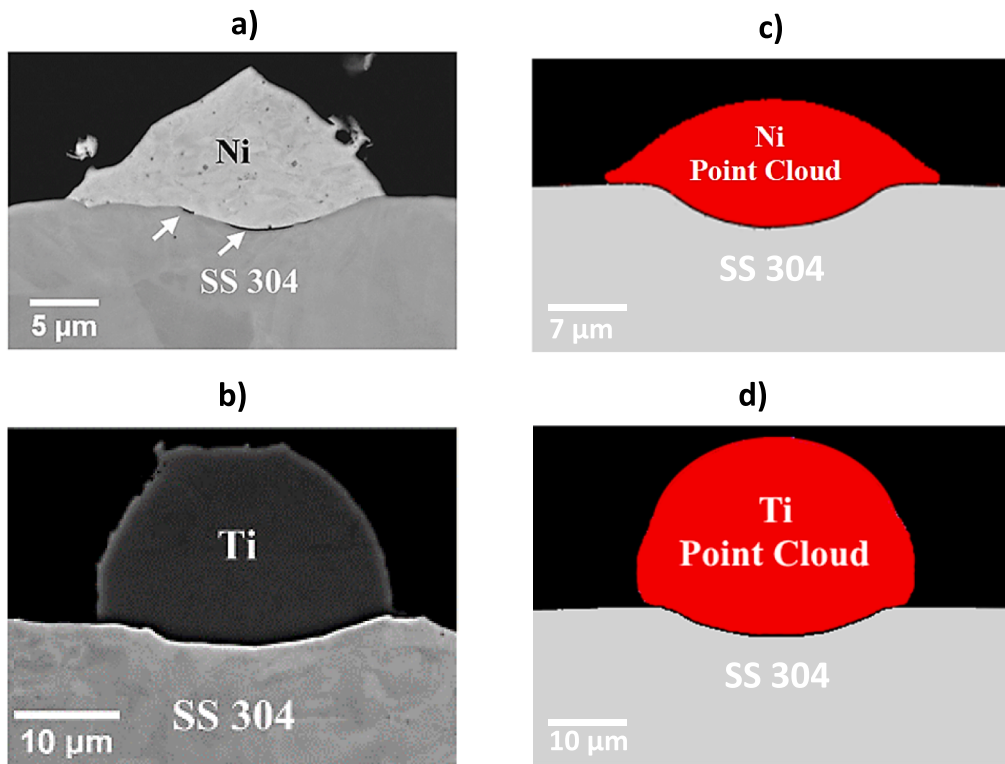


Fig. 3. Comparison of deformed particle shapes from: a) – b) previous experiments [30], and c) – d) hybrid simulations. Images corresponds to that of 25 μm Ni and 30 μm Ti particles impacting at 500 m/s unto SS 304 substrate.

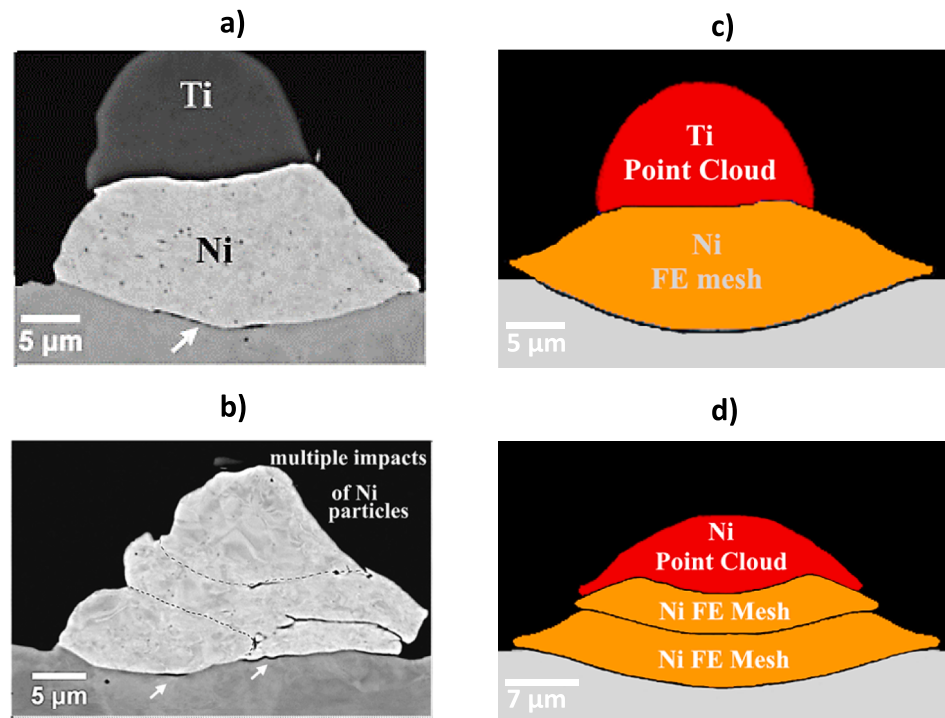


Fig. 4. Comparison of deformed particle shapes from: a) – b) previous experiments [30], and c) – d) hybrid simulations. The image for double particles corresponds to 25 μm Ti and 30 μm Ni particles impacting at 500 m/s. The image for triple particles corresponds to 25/22/18 μm Ni particles impacting at 500/546/610 m/s.

substrate with 500 m/s and 300 K when a gas pressure of 8 bar and gas temperature of 354 °C are used. For the same spraying conditions, 22 μm and 18 μm Ni particles will impact the substrate with 546 m/s and 610 m/s, respectively. Therefore, the initial impact velocities of 500 m/s,

546 m/s, and 610 m/s are considered for the triple particle case presented in Fig. 4d. The numerical simulation results converge with the PC containing at least 89,094 points. The deformation of the Ni and Ti particles on the PC-FE domains has been observed to reasonably

compare with that of the prior experiments [30]. The deposited particles deform into a more flattened structure, known as a “splat”, after impact. The impacting particle partially penetrates the substrate surface because of the strong impacting force created at the contact zone. From the previous experiments [30], the impact of a single 25 μm Ni particle results in a splat thickness of 12 μm and splat diameter of 23 μm (Fig. 3a). According to the current simulations (Fig. 3c), the maximum splat thickness and diameter for the single 25 μm Ni particle are obtained as 11 μm and 28 μm , respectively. For the single 30 μm Ti particle (Fig. 3b), the previous experiments [30] reveal a splat thickness of 19 μm and a splat diameter of 27 μm . On the other hand, the simulations in Fig. 3d show a splat thickness of 23 μm and a splat diameter of 37 μm . It is important to note that slight variations in splat sizes and morphologies are observed in Fig. 3. When comparing the numerical and experimental results presented in Fig. 3 and Fig. 4, some variations in maximum splat dimensions are expected. This could occur because it is not certain if the cross section (shown in Figs. 3 and 4) is created at the plane that intersects with the splat centroid; as a result, relying solely on the cross section views to determine the maximum splat dimensions might make it difficult to compare numerical and experimental data accurately. Additionally, for the double and triple impact cases presented in Fig. 4, it is evident that the work hardening of the previously deposited Ni particles influences the deformation of the subsequently impacting particles, as discussed in previous studies [30]. Even though the Johnson-Cook (JC) model incorporates this work hardening effect, the model might need to be further calibrated through several multi-particles experiments to account for this phenomenon appropriately [36,37]. Nevertheless, the current simulation results show that the deformation behavior of newly impacting particles is influenced by the work hardening of the substrate and previously deposited particles. For the double impact case, the cross-section image (in Fig. 4a) shows the maximum splat diameter over the maximum thickness for the Ni and Ti particles, respectively, is 2.31 and 1.50. On the other hand, the corresponding ratios from the simulations are 2.5 and 1.79 for the Ni and Ti particles, respectively. The triple impact simulation case (in Fig. 4d) shows the maximum splat diameter over the maximum thickness of 8, 7 and 2.14 for the first, second and third impacting particles, respectively. The cross-section image (in Fig. 4b) demonstrates that the corresponding

ratios for the three impacting particles are 5, 5, and 1.45. The deviations between the maximum splat dimensions predicted numerically and from the earlier research [30] are because of the simplifying simulation assumptions, such as the: i) negligence of substrate surface roughness, ii) adoption of a perfectly spherical particle, iii) small differences between the experimental and simulation particle impact velocities and misalignments. Consequently, the differences between the numerical and experimental splat dimensions are more visible for multiple impact cases due to the difficulties in maintaining a perfect condition for particles impact in the experiments. Although not very substantial, the variations between the particle deformation characteristics found through numerical and experimental analysis cannot be attributed to any inaccuracies in the numerical simulation.

The splat shapes and sizes predicted with the hybrid approach are also compared with that of three-dimensional (3D) arbitrary-lagrangian-eulerian (ALE) simulations performed under the same spraying conditions (Fig. 5). There are apparent minor differences in the splat sizes and morphologies predicted with the two different methods. For the single Ni particle study (Fig. 5a and 5c), the maximum splat diameter over the maximum splat thickness is estimated to be 2.55 and 2.17 with the hybrid and ALE approaches, respectively. For the triple impact cases (in Fig. 5b and 5d), the comparable ratios are 8, 7, and 2.14 using the hybrid method and 6, 6, and 2.33 using the ALE approach. The particles deform a little more with the hybrid approach, but the predictions from the two methods are similar and reasonably compare well with the results of the earlier experiments [30]. The resistance of particle deformation in the ALE simulations can be attributed to the increasing deformation resistance caused by the remeshing and associated element distortion. Additionally, pseudo-particle boundary conditions for the SPH domains, and the minor geometrical variations between the PC and converted FE domains may have contributed to the slightly higher particle deformation obtained using the hybrid approach. Table 2 shows the flattening ratios obtained with the two modeling approaches and data from previous experiments on Ni and Ti coatings [29,30]. Additional plots showing a direct comparison of the numerical results obtained with the hybrid and ALE approach are given in Appendix A (Fig. S4). The flattening ratio, i.e., $f = 1 - h_{\max}/D_0$ (where h_{\max} is the maximum splat thickness and D_0 is the initial particle diameter) is used

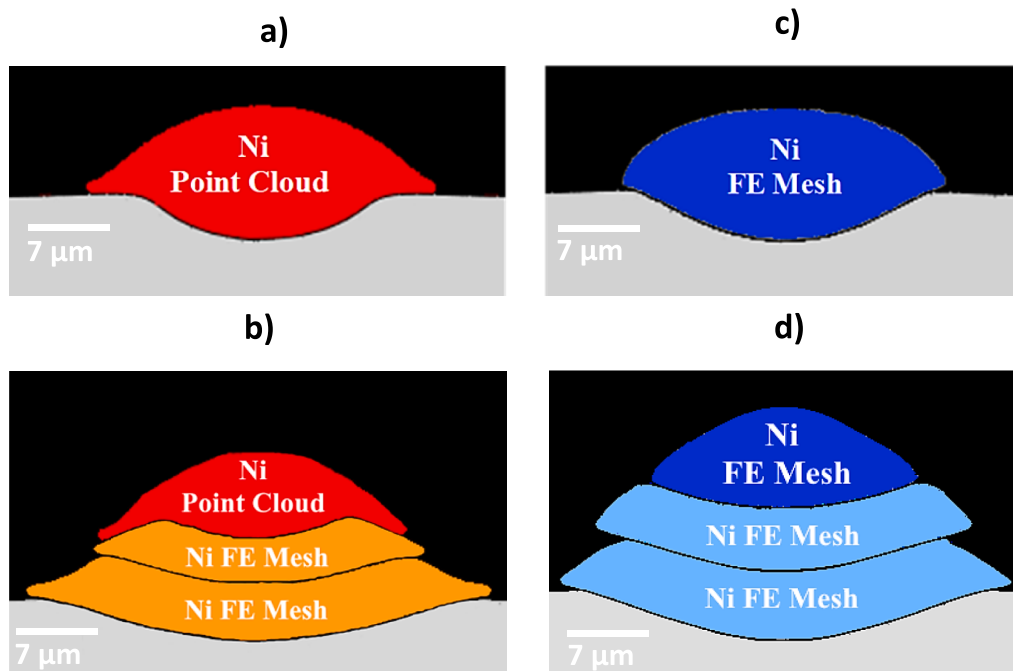


Fig. 5. Comparison of deformed particle shapes as obtained with the: a) – b) hybrid and c) – d) ALE approaches. The image for the single particle corresponds to 25 μm Ni particle impacting at 500 m/s. The image for triple particles corresponds to 25/22/18 μm Ni particles impacting at 500/546/610 m/s.

to represent the extent of plastic strain during the impact deformation of particles. It can be observed that the flattening ratio varies for each particle in the cases involving the impact of multiple particles. The flattening ratio remains higher for the first or second impacting particles which are in direct contact with the substrate depending on which particle has a higher impacting kinetic energy. For the single impact study (i.e., cases A and B in Table 2 and Fig. 3), Ni appears to have a larger flattening ratio. This is because the Ti particle has a larger diameter and higher yield strength compared to the Ni particle. Similarly, the double impact study (i.e., case C in Table 2 and Fig. 4a and 4c) indicates that the Ni particle exhibits a slightly higher flattening ratio than the Ti particle. At the same time, the triple impact study (i.e., case D in Table 2 and Fig. 4b and 4d) demonstrates that the second particle exhibits higher flattening ratios in comparison to the first and third impacting particles. This results from the diversity in the kinetic energy of the impacting particles, the work hardening effect and the unequal particle deformation brought on by the complex shape of previously deposited particle layer. Moreover, it is observed that the flattening ratios obtained with the hybrid approach are closer to that of the experiments than that of the ALE simulations because of the limitations of the ALE and SPH methods mentioned earlier. Nevertheless, the flattening ratio values obtained with the current approach compare reasonably well with that of the ALE simulations and the previous experimental observations [30,36]. Due to the previously mentioned uncertainty around the experimental parameters and the rationale for adopting simplifying modeling assumptions, minor deviations in the flattening ratios are expected. Table 3 compares contact parameters obtained with the two numerical approaches mentioned earlier. A fair comparison can be seen in the contact parameters for the single Ni particle. Nevertheless, the observed deviations can be insignificant, considering the computational benefits of the hybrid approach. With the hybrid approach, the simulation run time for a single Ni particle impact is only about 2 h with serial processing and the Dell workstation of 24 cores of Intel processor, 64 GB RAM, and 2.0 GHz (Table 4). Accordingly, the simulation run time was 38 and 51 h for the double and triple particle impact cases, respectively. This includes a PC processing code run time of about 10 min per splat. Due to the considerable increase in the number of finite element grid points brought on by the addition of the previously deposited particles FE mesh, the simulation run time for the subsequent impact simulations increase parabolically (Table 4). The stable time step size is further restricted by the refine mesh around the splat boundaries, which adds to the increased simulation time. On the contrary, the simulations with the ALE method and parallel processing took around 23.5, 64.5, and 114.0 h for the impact of single, double, and triple particles, respectively. This becomes far more than the computational run times of the hybrid simulations. In addition to computational benefits, the hybrid technique combines the advantages of Lagrangian and Eulerian schemes as revealed in the prior study [19]. In multi-particle and multi-layer SPH simulations, the method reduces numerical difficulties associated with tensile instability, high memory usage and poor contact interactions. When using Lagrangian FE schemes, it minimizes the problem of poor mesh distortion. In contrast to Eulerian schemes, it eliminates the boundary coalescence issue and makes it possible to distinguish between interactions among interparticle

boundaries. Therefore, the hybrid simulation approach for CS deposition offers some benefits over the existing simulation methods which needs not to be overlooked.

3.2. Influence of deposition parameters on particle deformation characteristics

To study the dynamics of particle deformation during the CS process, the evolutions of equivalent plastic strain, temperature, and von Mises stresses are tracked for the simulation cases involving the impact of single and multiple Ni particles onto the SS304 steel substrate. The particle sizes, impact velocities, and temperatures varied over the range: 5 μm – 60 μm , 125 m/s – 1250 m/s, and 300 K – 600 K, respectively. Different particle morphologies are also considered, including spherical, hollow spherical, oblate, angular, flake-like, and rod-like. Fig. 6a and 6b demonstrate the equivalent plastic strain distribution during the deposition of the Ni particles. The contour plots show that the distribution of the equivalent plastic strain is non-uniform and nonlinear throughout the dimensions of the particles and substrate, consistent with previous findings on Ni/Ti particle deposition using the ALE scheme [30] (Fig. 6a and 6b). This is attributed to the unequal particle deformation along the vertical and horizontal directions. For the first impacting particle, the equivalent plastic strain magnitude increases with the depth of the deposited splat until reaching its maximum value at the regions near the coating-substrate interface (Fig. 6e). In line with the direction of impact velocity, the deformation and distribution of equivalent plastic strain appear symmetrical along the vertical axis as revealed in the previous study [30]. The magnitudes of equivalent plastic strain increase with increasing particle impact velocities and initial temperature (Fig. 6d and 6e). Moreover, the plastic deformation becomes higher towards the edges compared to the central region of the interface zone, as commonly noticed in CS literature [19]. This is because of jetting out phenomenon caused by the adiabatic shear instability and sliding motion of particle interfaces due to the fast-propagating shock waves [19,30]. Recently [37], it has been argued that the impact velocity required to produce adiabatic shear instability is insufficient to generate splat bonding. Instead, splat bonding can happen without adiabatic shear instability because of the interaction between the strong pressure waves and the free surface of the splat edges. As a result, the bonding of particles depends on the relationship between the critical velocity and the bulk speed of sound. Therefore, the formation of jet, hydrodynamic plasticity, and associated sliding motion are all beneficial for the coating adhesion [19,30,37]. In addition, removing the oxide layers on the particles' surface due to the sliding/plastic deformation of the particle–substrate interface aids in the bonding of splats [19,30]. The jetting out phenomenon is, therefore, more pronounced for the particle closest to the substrate interface (Fig. 6a – 6c), even though the jet-out lengths in Fig. 6a and Fig. 6b are insufficient to produce adequate bonding with the particle impact velocity of 500 m/s, which is slightly lower than the critical particle velocity presented in Table S1 [30].

Upon the impact of the second Ni particle, the convex shape structure of the predeposited Ni particle transforms into a concave one (Fig. 6a – 6c). The highest plastic deformation occurs near the top region of the predeposited Ni splat. These observations were also made with respect to multiple Ni and Ti particle deposition using the ALE simulation approach [30]. In contrast to observations made at low impact velocities (i.e., 500 m/s), the deformed shape of the newly impacting particle at 1000 m/s takes the form of a round ellipsoid due to the spreading resistance caused by its high penetration depth (Fig. 6c). Consequently, there are apparent differences in the aspect ratio (i.e., $AR = \frac{r_1}{r_2}$; here r_1 and r_2 are the maximum and minimum radial dimensions) of the deformed Ni particles (in Fig. 6a and Fig. 6c) as reported in previous studies [30]. The aspect ratios are estimated at 2.95 for the first particle and 2.90 for the second particle for an impact velocity of 500 m/s (Fig. 6a). For the impact velocity of 1000 m/s, the corresponding ratios

Table 3

Comparison of contact parameters obtained for a single Ni particle impacting at 500 m/s as obtained with the current approach and ALE model. The Ni particle diameter used is 25 μm .

Particle Types	Contact parameters	
	Hybrid	ALE
Contact pressure (MPa)	777.0	815.0
Max. von Mises stress	778.0	923.0
Plastic radius (μm)	17.0	19.0
Max. penetration depth (μm)	6.2	8.3

Table 4

Comparison of the computational efficiency, accuracy, and time step size for the hybrid and ALE simulations of single, double, and triple particles impacting on SS304 substrate.

	Hybrid			ALE		
	Ni	Ni/Ni	Ni/Ni/Ni	Ni	Ni/Ni	Ni/Ni/Ni
#Elements	270,594	359,688	448,782	270,594	359,688	448,782
Solver Sequence	Serial	Serial	Serial	Parallel	Parallel	Parallel
$\Delta t_{average}$ (ns)	0.0052	0.0006	0.0006	0.0045	0.00092	0.00043
C _r (hours)	1.91	37.72	51.0	23.5	64.5	114.0
T _{max} (K)	480	545	600	477	520	570
σ_{v-max} (MPa)	778	870	916	923	856	920
ϵ_{max}	0.58	1.53	2.00	0.61	1.62	2.11

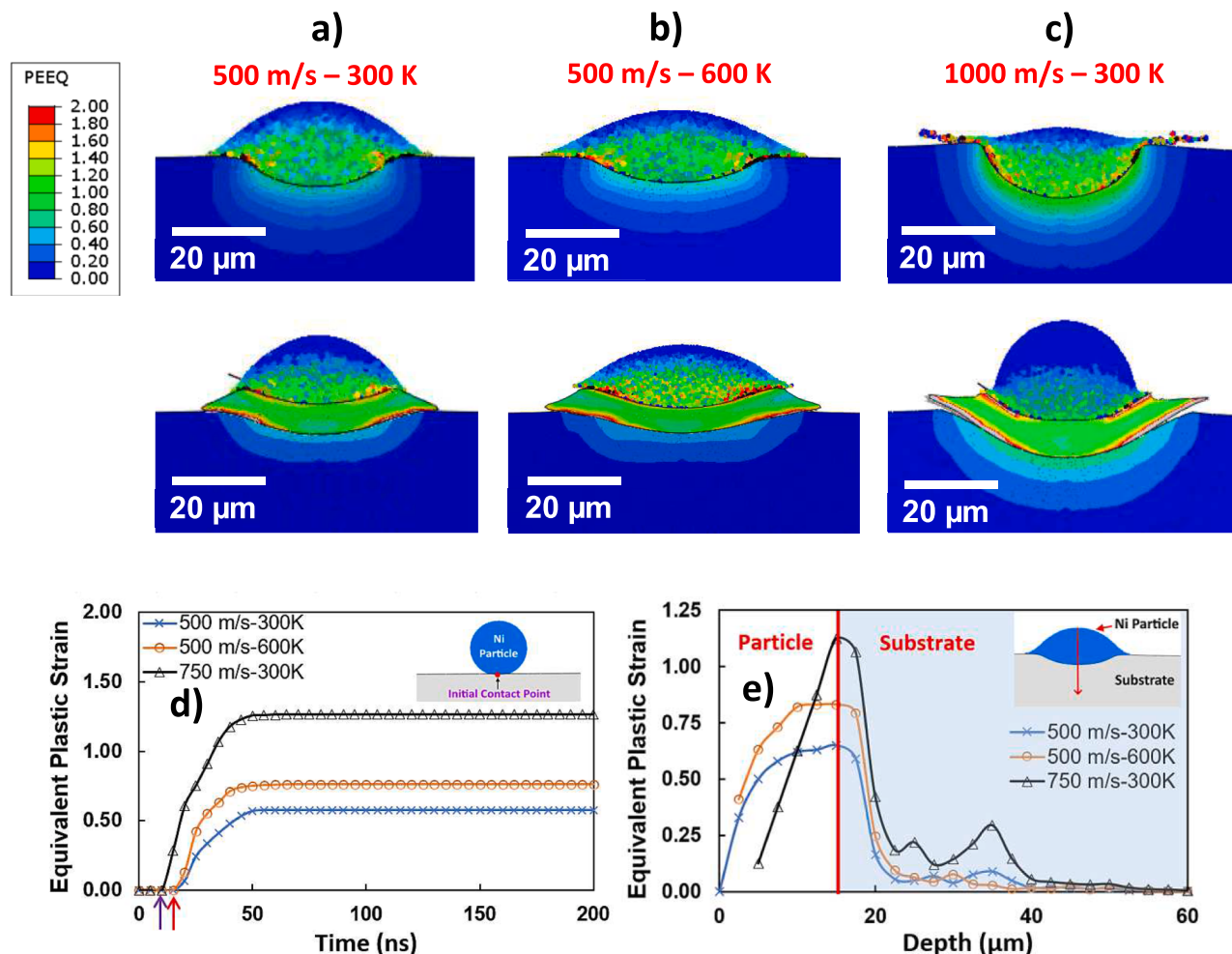


Fig. 6. The equivalent plastic strain distribution for 25 μm Ni particles: a) impacting at 500 m/s and 300 K, b) impacting at 500 m/s and 600 K, and c) impacting at 1000 m/s and 300 K. d) The equivalent plastic strain variation with: d) time, and e) depth are also shown for the single particle impact cases.

are 2.40 for the first particle and 1.68 for the second particle (Fig. 6c). Since the crater formation is favorable during CS deposition, the localized plastic deformation within the cratered region could further enhance the mechanical interlocking or strength at the mating boundaries, as stipulated in previous research [19]. The maximum penetration depth for the cratered region increases with increasing particle kinetic energy. Due to enhanced plastic deformation and the thermal softening effect, the Ni particle penetration depth quickly rises at the initial stage of impact deformation [19,30]. However, as the impact deformation process progresses, the work hardening effect assists the particle in penetrating further into the substrate, as observed in previous experiments [19,30]. Fig. 6d shows the temporal evolution of equivalent plastic strain developed at the first point of contact between the single Ni

particle and substrate surface. Rapid deformation of the particles and substrate can be observed in Fig. 6d. This occurs due to the high kinetic energy of the impacting particles attributed to the high-velocity gas flow out of the spray gun. The particle deformation occurs within the nanoseconds range, leading to highly localized strains forming in a quasi-adiabatic state. The maximum equivalent plastic strain increases non-linearly to a very high value during the impact and spreading period. It later stabilizes to a constant value. For a single particle, the equivalent plastic strain remains higher at the interface region as compared to the top and mid-section regions (i.e., about $\epsilon_{pl} = 0.6$ at 50 ns for the single Ni particle at 500 m/s and 300 K in Fig. 6e). For the second and subsequent impacts, the strain field becomes redistributed across the particle bodies such that the inter-splat boundaries and edge regions of the

coating material develop local temperature maxima; hence, an oscillatory trend is predicted, as earlier shown in Fig. 6a – 6c. Higher plastic deformations are observed at higher impacting velocities and larger particle sizes, and vice versa. The occurrence of complex phenomena such as local stress concentration, strain hardening, and thermal softening contributes to the high localization of strain field spotted in Fig. 6. The transformation of energy during the impact and deformation of cold sprayed particles is often described with the aid of the energy balance equation [28]: $E_{k_1} = E_p + E_{k_2} + E_e + W_T + E_{loss}$; here: E_{k_1} is the impacting particle kinetic energy, E_{k_2} is the rebounding kinetic energy, E_p is the energy dissipation due to plastic deformations, E_e is the recoverable elastic strain energy, W_T is the total external work done by the system, and E_{loss} is the energy dissipation terms for losses associated with other mechanisms such as particle erosion, friction, sound, and viscous damping forces, which are all negligible here. The average of equivalent plastic strain developed within the impacting particle increases non-linearly with the particle diameter and impact velocity (Fig. 7a). This is because of the increase in impacting particle kinetic energy or higher degree of thermal softening during particle deformation. The average equivalent plastic strain developed in particles pre-heated to 600 K is considerably more than when impacting particle velocity is doubled; thus, improved Ni particle attachment to the substrate may result from the rise in plastic deformation brought on by

thermal softening or particle preheating as previously discovered [17]. It is observed that the average plastic strain for the particles impacting at 1000 m/s is slightly affected by mass loss due to splashing or extreme jetting. The particle flattening ratio (in Fig. 7b) increases with increasing particle diameters and begins to decline for larger size particles because more energy is used to achieve deeper substrate penetration by the larger size particles. Due to high thermal softening effect, the flattening ratio increases with increasing particle initial temperature. Furthermore, for higher ranges of the particle impact velocity considered here, the particle flattening ratio decreases with increasing impact velocities. This is as a result of the spreading resistance caused by deeper substrate penetration of the particles. Nevertheless, the adhesion strength will be higher for coating particles deposited under high spray conditions because of higher peening forces, higher plastic deformation and lower elastic strain recovery. According to the numerical simulations, the flattening ratio map for particles of different sizes impacting at different initial impact velocities and 300 K is shown in Fig. 7c. Low impact velocities (i.e., less than 250 m/s) and low particle size result in less severe deformation of the impacting particle; in which case, a significant portion of the impacting kinetic energy is converted into elastic recovery/rebounding kinetic energy. Consequently, the Ni particles might rebound from the substrate surface at low impact velocities due to higher elastic rebound forces and lower flattening ratio. For the moderate impacting velocities/particle size, rebounding does not occur, and

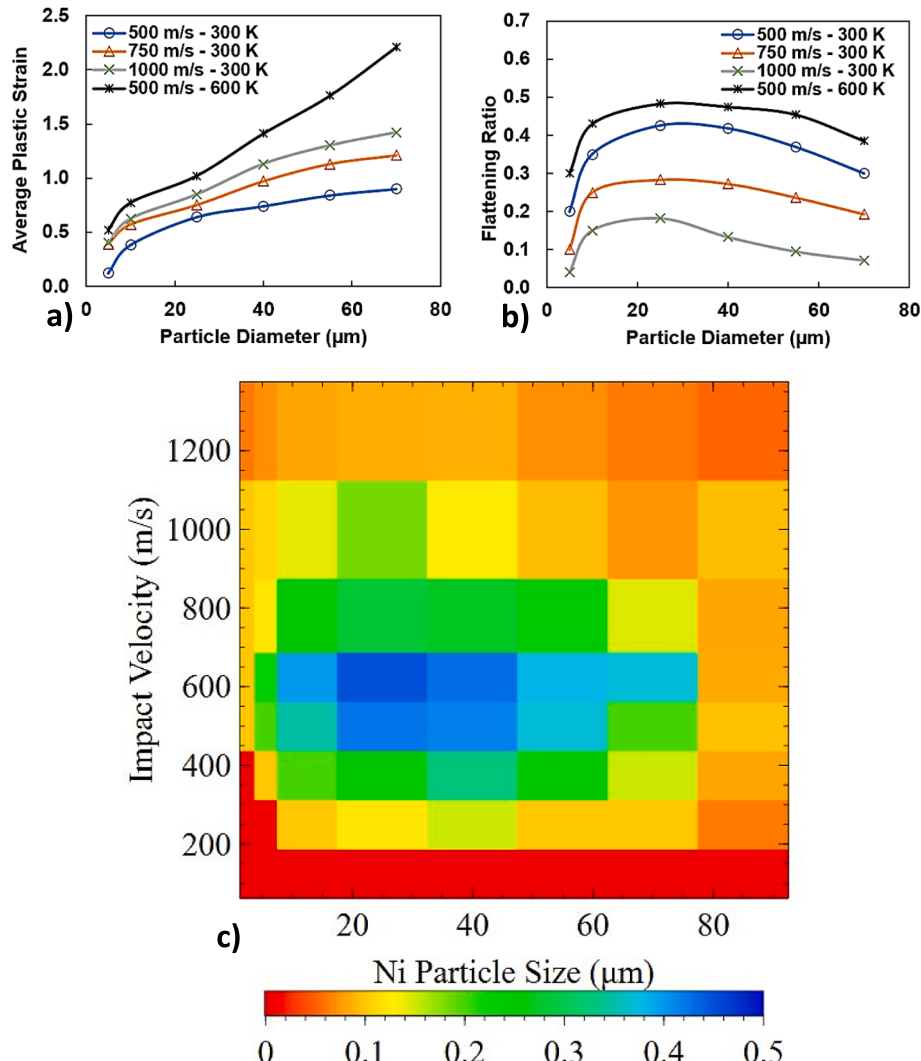


Fig. 7. a) Average particle plastic strain and b) flattening ratio variation with the particle diameter and impact velocities. c) Flattening ratio map for different particle size and impact velocities for spherical Ni particles impacting at 300 K unto SS304.

the flattening ratio becomes more favorable for splat bonding (Fig. 7c). At the other extreme, which is where impacting velocities are higher (i.e., > 1250 m/s) and particle sizes are larger, bonding might be adequate. However, the large loss or erosion in particle mass may cause the deposition efficiency to decrease; in which case, much of the particle material splashes away.

Fig. 8a and 8b show the temperature distribution and von mises stress field developed across the particle and substrate domains. The temperature distribution is also non-uniform and symmetrical, as observed in the plastic strain case. The formation of heat localization zones across the interfacial boundaries can be observed. The temperature rise due to plastic heat dissipation increases across the depth of the coating splat until reaching the maximum value near the interface region, as commonly observed in CS simulations [19,30]. On the other hand, the temperature reduces with the depth of the substrate, as expected. Fig. 9a shows the temporal evolution of temperature at the initial point of contact. Initially, the temperature rises sharply until attaining a constant level, as observed for the case of the equivalent plastic strain (Fig. 9a). The temperature ceases to reduce towards the end of the particle deformation because the duration of deformation becomes too short (in the ns range) for heat dissipation via conduction, convection, or other mechanisms. Consequently, the temperature

evolution follows a similar trend as that of equivalent plastic strain with the highest values developed near multi-material and inter-splat boundaries (Fig. 9b). However, the previous research by Oyinbo et al. [32] show that the maximum temperature in Cu substrate decline by about 20 °C after particle deformation ceases. This is because of the extremely high thermal conductivity of Cu compared to SS304. The spatial distribution of temperature varies across the depth of the Ni splat thickness while reducing on the substrate side (Fig. 9b). For the first impacting Ni particle, the maximum temperature rise near the splat boundaries could not reach that of recrystallization, i.e., only around 470 K for the impact conditions at 500 m/s and 300 K (Fig. 8a & 9b). However, upon the second and subsequent impact, the temperature could reach 800 K, somewhat near the crystallization range (Fig. 8a and 9b). Moreover, for the case in which the particles were preheated to 600 K before impact, the maximum temperature reaches nearly 1000 K, which is still below the melting point of Ni. Even though the dynamic recrystallization process occurring at particle boundaries could improve the coating bond strength, preheating of the Ni particles before spraying needs to be kept within a reasonable range to mitigate the possibility of the evolution of grain size or new phases during cold spraying [38,39]. It is important to note that the recrystallization process is not incorporated into the current simulations. Recrystallization takes place under the

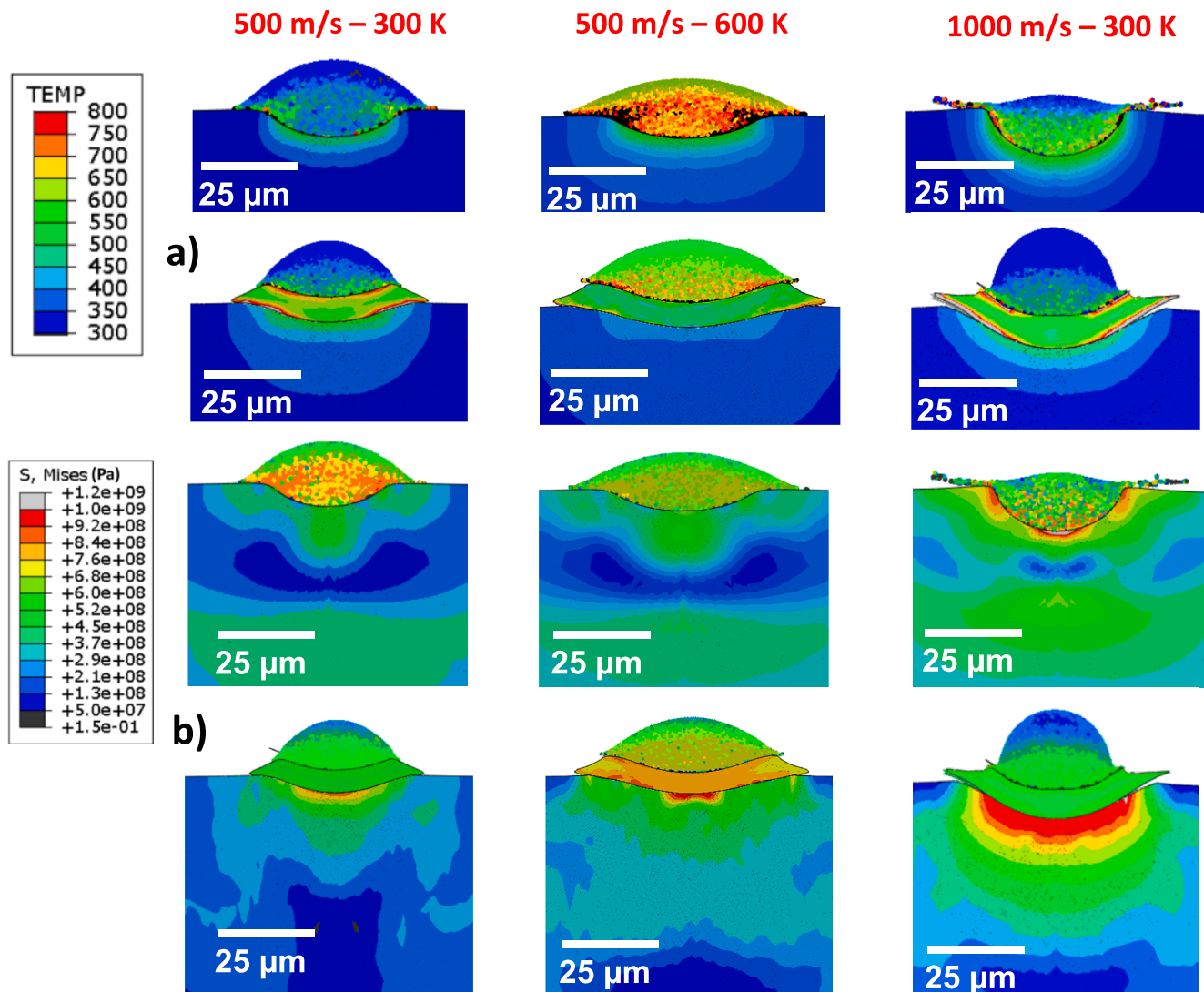


Fig. 8. The distribution of: a) temperature and b) von Mises stress for single/double 25 μm Ni particles impacting at 500 – 1000 m/s and 300 – 600 K. Particle jetting and mass loss is observed at 1000 m/s.

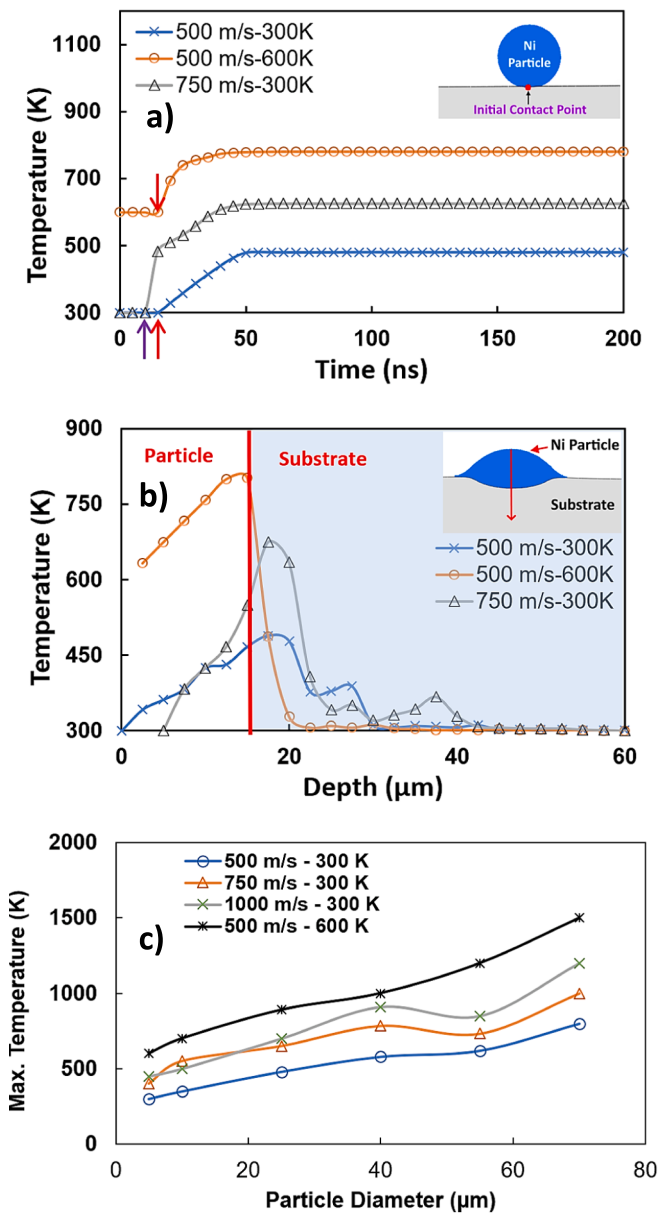


Fig. 9. a) The variation of temperature with: a) time, and b) depth at the initial point of contact for the single particle impact cases. c) The maximum particle temperature variation with the particle diameter and impact velocities.

combined influence of temperature, strain, and strain rate, all of which are impacted by dislocation formation; thus, incorporating the recrystallization effect on particle deformation requires the coupling of multiple scale simulations. Nevertheless, the higher thermal diffusivity in heated particles can promote localized shear instability and increase coating adhesion strength, as revealed in a recent study [17,40]. The maximum temperature rise during the particle deformation increases with increasing particle diameter and impact velocities due to higher plastic heat dissipation (Fig. 9c). This is obvious since CS deposition happens very fast, and previous research [19] shows that 90 % of plastic deformation energy is dissipated as heat; thus, higher impacting energy promotes plastic heat dissipation. Even though it is noted that the particle mass loss affects the temperature evolution for particles impacting at higher velocities, increasing the particle diameter allows for a lower increase in temperature rise within the particle body compared to when the impact velocity or impact temperature is high. This is because of more plastic dissipation in the particle, substrate, or both. It is also

observed that the temperature distribution within the cratered region of the substrate remains uniform along the circumferential direction, as previously observed [32]. The von Mises stress field distributions for the various cases are shown in Fig. 8b. Highly complex stress fields are developed within the particle and substrate bodies. Higher stresses are developed in the deformed region of the particles due to increasing plastic deformation. Similarly, the particle edges and topmost areas develop tensile stresses partly because of the material jetting-out phenomenon, which tends to elongate the particle towards the extreme boundaries. For the first impact, high compressive stresses up to 800 MPa are developed near the interface region compared to its topmost portion, which develops around 350 MPa. For the second and subsequent impacts, the stresses in the first particle increased tremendously due to the peening deformation caused by the newly impacting particles. Fig. 10a shows the temporal variation of von Mises stress during the impact and particle deformation periods. At the onset of impact, very high (compressive) stresses are developed at the initial point of contact due to the propagation of fast shock (or stress) waves that die out with time in a wave-like fashion. It is well known in the CS literature that compressive residual stresses benefit the coating layer strength and adhesion [19]. The simulations predict that the stress waves propagation frequency can be as high as 50 MHz with an amplitude of about 100 MPa for the Ni particle impacting at 500 m/s and 300 K. For this particle, the maximum von Mises stress diminishes to an equilibrium state, maintaining a value of 380 MPa after a period of about 150 ns. This happens because of stress wave attenuation and relaxation due to plastic deformation, thermal softening, sliding motion, and eventual splats bonding. The stress state developed across the depth is equi-biaxial, with the highest values of stresses existing in the out-of-plane direction (Fig. 10b and 10c). This is consistent with the previous observations from the literature [19], which show the formation of an equi-biaxial residual stress field and the high dependence of the stress field on the local temperature distribution developed during plastic deformation. It is important to note that thermal-mismatch stresses are not considered when calculating residual stresses since both particles and substrates are solid, the temperature rise is not severe, and the cooling rate is relatively low. In future works dealing with multi-material deposition, it may be necessary to consider the mismatch stresses for the ceramic-metallic particle system.

The powder particle morphology strongly influences the microstructure of CS coatings [41]. This is because, unlike thermal spray, CS is a solid-state deposition process where particles do not melt during the inflight period; any change in shape causes changes in inflight particle kinematics and plastic deformation. Due to the fast and localized nature of material deposition, this could not be easy to study experimentally. The hybrid computational approach proved an effective modeling tool for such a study. Therefore, in this regard, additional simulations are carried out to further demonstrate the ability of the proposed hybrid approach in the prediction of the dependence of the coating layer formation and evolution characteristics on the morphology of impacting particles. Fig. 11a shows the distribution of equivalent plastic strain after the sequential impact of three Ni particles with an equivalent volume of $8.181 \times 10^{-15} \text{ m}^3$. Particles of various morphologies, such as spherical, hollow spherical, oblate, angular, flake-like, and rod-like shapes, are considered. The aspect ratios of the corresponding particles are (i.e., $AR = \frac{r_1}{r_2}$; here r_1 and r_2 are the maximum and minimum radial dimensions): 1, 1, 1.67, 1.31, 2.41, and 6.17, respectively. For simplicity and ease of results comparison, sequential particle impact is considered. However, in practical CS equipment, the particles impact at random locations on the substrate surface. Moreover, the initial particle impact velocities and temperatures are the same for all three particles, i.e., 500 m/s and 300 K, respectively. For the same impact conditions, the plastic deformation is grossly affected by particle morphology (Fig. 11a). A non-uniform plastic strain distribution is developed in the particle and substrate domains. The maximum impacting particle

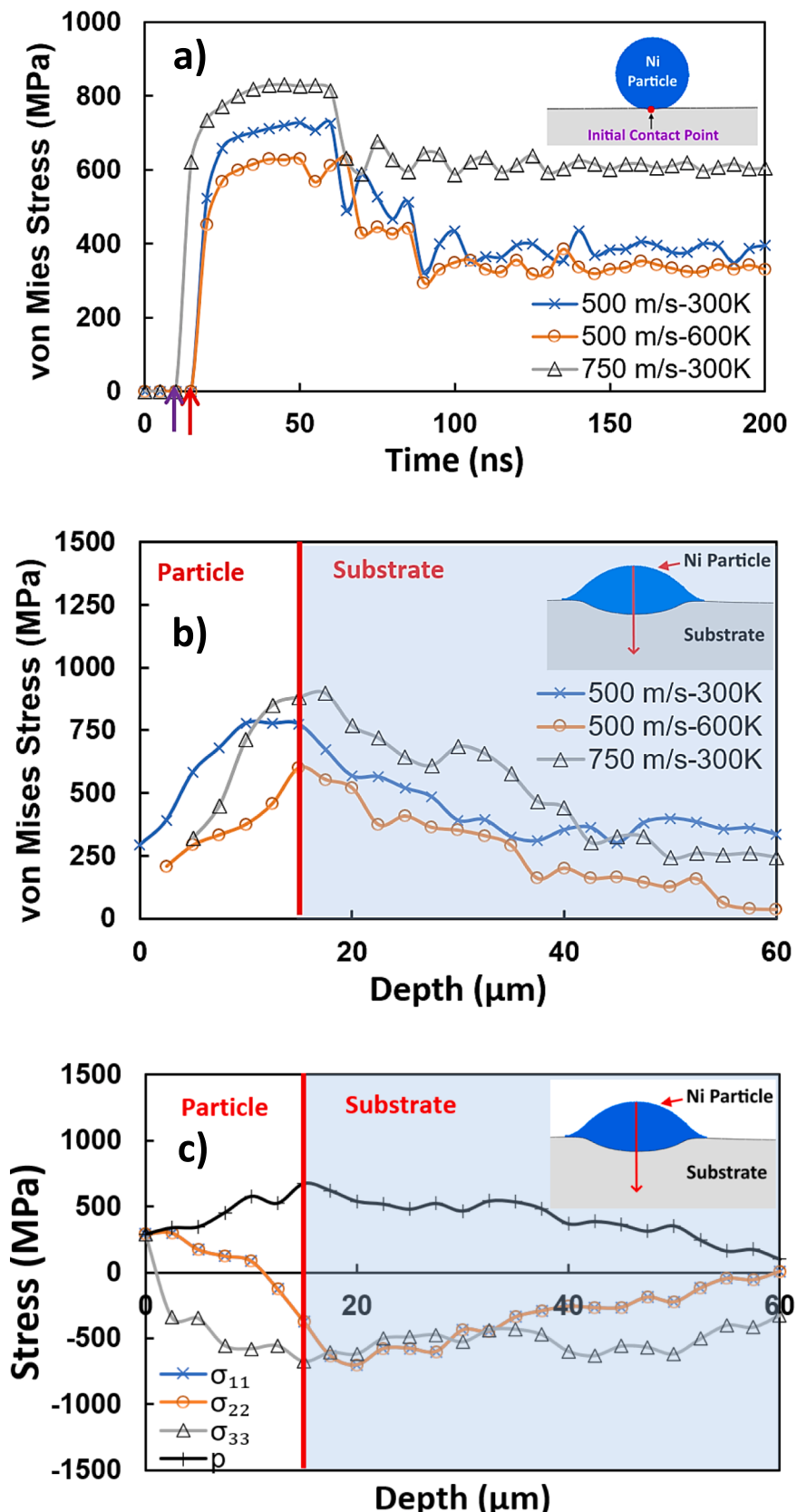


Fig. 10. A) The variation of von Mises stress with: a) time, and b) depth at the initial point of contact for the single particle impact cases. c) The variation of stress components with the depth of coating and substrate layers. σ_{11} and σ_{22} are in-plane normal stresses, while σ_{33} is the stress along the impact direction.

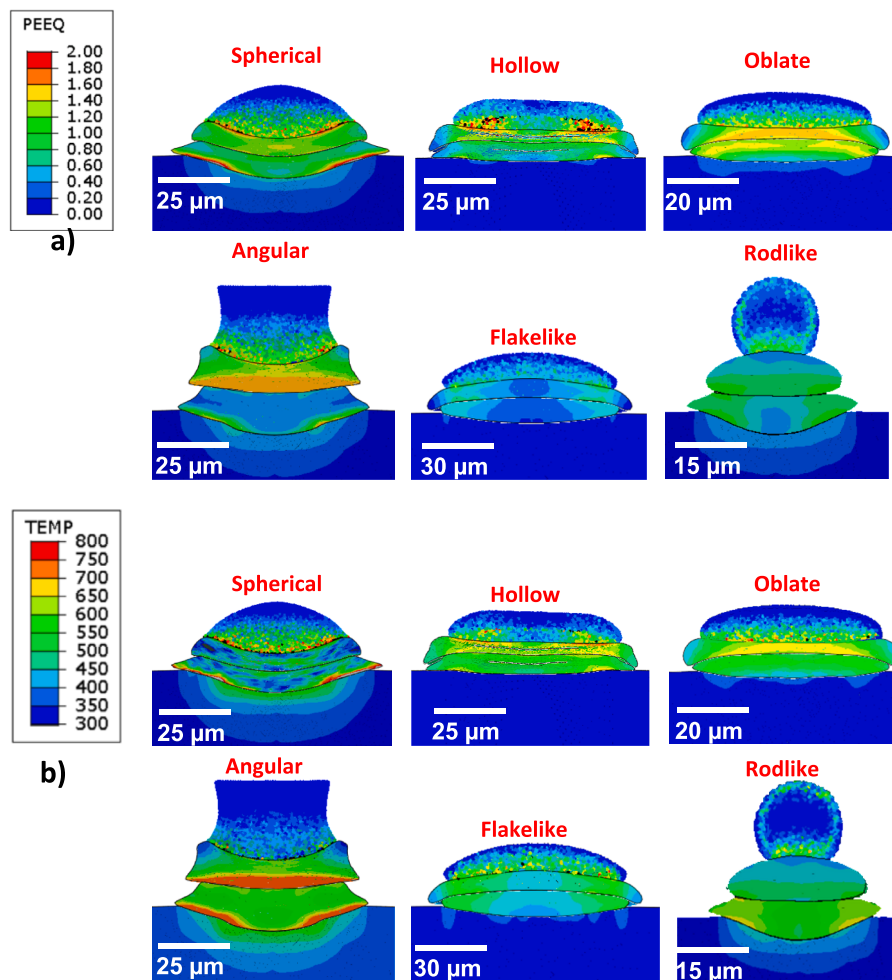


Fig. 11. The distribution of: a) equivalent plastic strain and b) temperature for triple Ni particles of various shapes impacting on SS304 at 500 m/s and 300 K.

deformation occurs during the deformation of the hollow spherical particles (i.e., $\epsilon_{pl} > 2$ due to hole deformation) followed by the other particle types in the following order: ϵ_{pl} 2 for spherical, ϵ_{pl} 1.8 for oblate, ϵ_{pl} 1.7 for angular, ϵ_{pl} 1 rod-like and ϵ_{pl} 0.8 for flake-like particles. The reasons for the particle morphology effects on the impact deformation behavior are explained as follows. The hollow spherical particle is more deformed and collapses into a thin disk-like splat structure before the particle spreading phase is over. The hollow spherical particle is highly impacted by the interior hole feature (or air gap). However, the impact of the hollow spherical particles results in a very shallow substrate penetration depth. Similar to hollow spherical particles, bulk spherical particles experience significant deformation upon impact, exhibit greater flowability and reveal severe tamping action on the substrate. This results in more uniform deformation of the substrate and deeper penetration depth. The interface created by the spherical particles shows a wavy-type morphology, indicating the possibility for stronger mechanical interlocking (or adhesion strength) between the spherical particles and substrate, as revealed in a recent study [42]. Moreover, the coating porosity is expected to be minimum with the spherical particles due to their high flow ability brought on by their curved spherical and symmetrical structure. The oblate particles have some features of spherical particles, such as good flow ability and appreciable particle deformation. However, the lower penetration depth into the substrate might affect the bond strength of oblate particles. Angular particles resulted in a highly complex and uneven deformation that makes it difficult for effective spreading of particle material, even though the impacting particle showed a higher tendency for sliding motion during

the deformation period. This is attributed to their complex shape feature, highly localized stress concentration, and inter-particle friction, as reported in the earlier work [42]. As a result, angular particles should exhibit lower flowability during impact deformation. The rod-like and flake-like structures have the least deformation and might not stick well and instead undergo rigid body rotation or fragmentation due to their high aspect ratios. A prior investigation by Shockley et al. [43] confirms that essential coating properties, such as wear resistance, are significantly influenced by particle morphology. It has been discovered that spherical particles significantly improve the wear resistance of cold-sprayed coating more than angular ones [43]. Furthermore, a powder blend of uniform particle morphology results in a denser and stronger coating layer than a powder with mixed morphologies [44]. As mentioned earlier, the irregular shape particles might display poor interfacial bonding, higher porosity, and the formation of angular-shaped pores. However, it is expected that the irregular shape particles could be accelerated more efficiently than spherical ones due to higher drag forces [45]; thus, leading to highly localized stress regions. In addition, the higher surface area of irregular particles compared to spherical ones could influence the chemical kinetics of reactive powders subjected to pre and post-deposition heat treatments [46,47]. Fig. 11b shows the temperature distribution developed after the CS deposition of different shape particles. The figures clearly show that particle deformation affects the evolution of temperature. The temperature distribution is non-uniform and strongly influenced by the complex interactions among particles, particle morphology, and process parameters which is challenging to evaluate experimentally.

3.3. Multi-layer particles deposition and coating layer growth

Further simulations are carried out utilizing varying particle characteristics and impact conditions to further test the suitability of the proposed approach in modeling CS deposition. The distribution of the equivalent plastic strain, temperature, and von Mises stresses are shown in Fig. 12a, 12b, and 12c, respectively. The splat interfaces develop highly localized plastic strain due to the thermal softening caused by

temperature evolution during particles deformation, as mentioned earlier (Fig. 12b). The severity of plastic deformation could be exacerbated by the impact of different shape particles at random locations on the predeposited coating material or the substrate surface. In that case, the plastic deformation of the multiple impacting particles becomes largely affected by the high displacement gradients developed during the deposition. The multi-layer particle deposition simulations show the typical complex-shape splat structures commonly seen in the

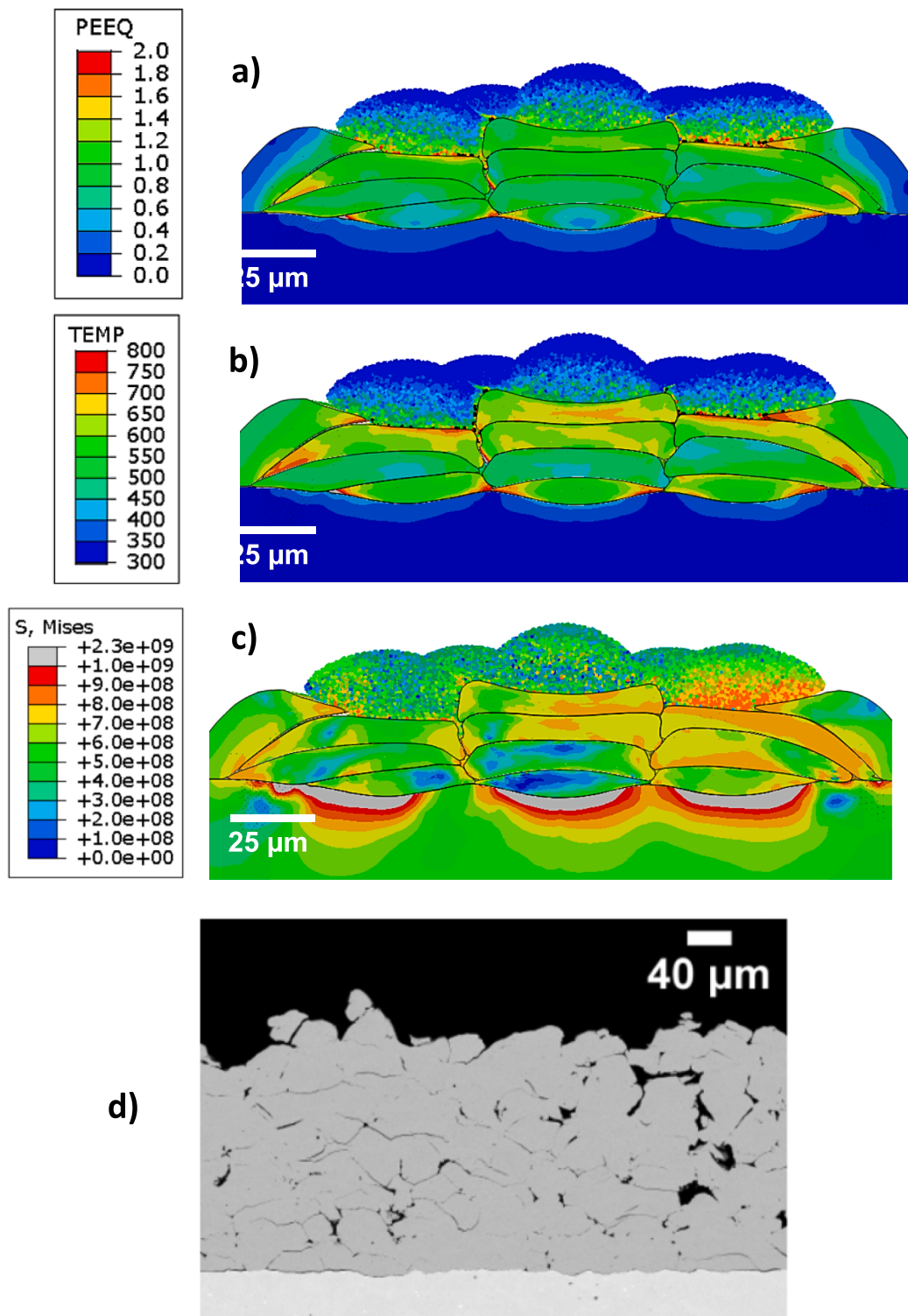


Fig. 12. Four-layer simulations showing splat morphology and: a) plastic strain, c) temperature, and c) von Mises stress for multiple particles impacting with random velocities and impact points. d) Splat morphologies obtained from previous experiments [48].

microstructure of cold-sprayed Ni coatings (Fig. 12d). The SEM images [48] in Fig. 12d demonstrate the basic features predictable from the multi-layer simulation, such as inter-splat boundaries, randomness in splat morphology and size, microcracking, voids, and highly rough surface. In addition, multilayer simulations could be used to evaluate the temperature, plastic strain, and residual stresses developed in the coating layer. As demonstrated in Fig. 12, the severely compressed particles are the ones that are directly in contact with the substrate or the ones that possess higher impacting kinetic energies and initial temperatures. The maximum equivalent plastic strain reaches as high as 1.5, 1.8, and 2.3, near the regions of the substrate interface, particle edges, and inter-splat boundaries, respectively (Fig. 12a). The temperature distribution formed during particle deformation shows that the large plastic heat dissipation and high thermal interphase resistance causes entrapment of heat within the particle boundaries (Fig. 12b). The maximum temperature rise within the coating layer is about 300 K. The temperature increases with the depth of the coating layer. Fig. 12c shows the von Mises stress field developed across the thickness of coating and substrate layers. Due to the large plastic strains developed during particle deformation, a highly complex residual stress field is developed across the dimensions of the mating bodies. The residual stresses are compressive within the coating layer; however, the stress developed across the edges and free surfaces were tensile to maintain the force balance during deformation. The stress field becomes non-uniform/nonlinear across the particle and substrates domains. The maximum von Mises stress developed in the coating and substrate layers are 750 MPa and 500 MPa, respectively. The stresses developed near the inter-splat interfaces/edges/curved regions are higher than particle interior or near-surface regions. Even though the particle deformation occurs in three dimensions, the computational run time is less than 72 h using 24 cores of Intel processor, 64 GB RAM, and 2.0 GHz from a Dell workstation. This indicates the high computational efficiency that can be achieved with the hybrid approach while noting that the typical run time for 3D triplet-particle impact using FE-based schemes is about 114 h. Modeling multiple particles deposition could lead to highly intensive simulations when the popular numerical schemes such as the ones developed from Lagrangian, Arbitrary-Lagrangian-Eulerian (ALE), and Coupled-Eulerian-Lagrangian (CEL) formulations, as pointed out in previous work [19]. Hence, the hybrid approach could be a more effective numerical methodology for optimizing CS deposition parameters and coating layer characteristics. It can capture the local particle deformation during deposition at lower computational costs. Furthermore, the approach could be more efficiently used to study coating layer thickness evolution and deformation mechanism when Ni particles impact on highly rough or curved substrate surface geometry. It can also be a viable tool for predicting particle grain size and morphological changes critically linked to temperature and plastic strain evolution within the impacting particles. The lower computational costs and its ability to handle complex geometries could allow the use of the hybrid approach to generate the computational microstructure or synthetic data needed to employ artificial intelligence in the advance design and optimization of cold-sprayed composite structures [49,50]. The final mechanical properties of the simulated coating layer (such as hardness, elastic modulus, strength, wear resistance, etc.) could be predicted through computational homogenization of computational microstructure developed via the hybrid simulations. The hybrid approach could be used to develop a coating deposition simulation module for designing and optimizing of CS coating process via effective prediction of the thermo-mechanical deformation developed during the process. The new approach will apply to the design of composite parts made via cold spray or other additive manufacturing processes. Most commercial FE packages (such as ABAQUS and ANSYS) have the capability for mesh-to-particle conversion modules for the simulation of large deformation problems. However, the inverse package, i.e., particles-to-mesh module, is missing and could be useful in solving problems where stability limitations necessitate deformed point cloud conversion back to the FE

mesh. While the proposed hybrid approach leverages the advantages of both meshless and meshed Lagrangian schemes, it has some of the limitations faced with the methods mentioned earlier [19], such as: i) the meshing of deformed particle regions with a fine mesh might lead to increased computational time for simulations involving multiple coating deposition, ii) the tensile instability problem affects the accuracy of particle deformation characteristics at very high impact velocities, iii) the default contact interactions formulation between SPH and FE domains may not fully capture interfacial deformation across the mating boundaries due to the use of pseudo-particles. Nevertheless, the limitations can be the subject of future research work in this field.

4. Conclusion

The present study presents a physics-based hybrid numerical approach for modeling the cold spray (CS) deposition of the Ni coating layer on the SS304 substrate. The method integrates smooth particle hydrodynamics (SPH) and finite element method (FEM) to model the evolution of temperature, plastic deformation, and residual stress during particle impact and coating layer buildup. The SPH is used to compute temperature rise and particle deformation during the high-velocity impact process on the point cloud domain. The FEM predicts the temperature rise and subsequent deformation within the predeposited coating or SS304 substrate layers on a finite element grid. Novel combinations of point cloud processing algorithms are used to convert the point cloud of deformed particles into high-quality FE mesh during the simulations. The effectiveness of the proposed hybrid approach is demonstrated via numerical simulations dealing with various combinations of particle and impact characteristics, such as varying particle sizes, spray temperatures, particle morphology, and impact velocities. The current numerical results are analyzed and validated by comparing them with other numerical schemes and previous experimental studies. The following conclusions can be derived from the current research:

1. The hybrid computational approach proved computationally efficient for predicting temperature and plastic strain distribution during the impact and interactions of multiple Ni particles across a wide range of CS parameters. Despite being three-dimensional (3D), the simulations took significantly less time than popular FE-based schemes like ALE and CEL methods. Specifically, simulations for depositing two and three Ni particles ran for about 38 and 51 h, respectively, whereas the ALE approach took around 64.5 and 114.0 h for the same cases. The hybrid method also mitigates several drawbacks in the other numerical schemes, including tensile instability, high memory utilization, poor inter-particle contact interactions, mesh distortion, adaptive remeshing processing, and coalescence of material interfaces. As highlighted in a previous review by Fardan et al. [19], the hybrid approach can be an alternative module for selecting CS process parameters and modeling materials behavior.
2. Severe plastic deformation and temperature buildup are observed during particle impact and deformation periods. The plastic deformation and maximum penetration depth into the substrate increase non-linearly with increasing particle kinetic energy. The highest equivalent plastic strain, reaching up to 2.0, is found near inter-splat boundaries, particle edges, and regions of the substrate interface. Furthermore, increasing the initial impact temperature of the particles from 300 K to 600 K leads to higher plastic deformation than doubling the impacting particle velocity (from 500 m/s to 1000 m/s).
3. The particle flattening ratio increases with increasing particle diameters and impact velocity. Still, it slightly reduces for larger particles or higher velocity ranges due to increased energy expenditure on substrate penetration. Low impact velocities (less than 250 m/s) and small particle sizes (less than 5 μm) result in lower flattening ratios and rebounding from the substrate surface. Moderate

- impacting velocities (450 m/s – 900 m/s) and particle sizes (10 μm – 60 μm) lead to favorable splat bonding conditions without rebounding. Higher spraying conditions (>1250 m/s and > 60 μm) might offer adequate bonding, but particle material loss or erosion from splashing or extreme particle jetting affects the deposition process. Additionally, in multiple particle studies, impacting particles closest to the substrate have slightly higher flattening ratios due to the interplay between work hardening and increased compression.
4. The maximum temperature rise in deposited particles increases with higher impact kinetic energy, reaching the recrystallization range without exceeding the melting point. Preheating particles to 600 K before deposition and subsequent impacts on previously deposited coatings contribute to this temperature buildup.
 5. Compressive residual stresses are mainly developed within the Ni coating splats, while tensile stresses form towards the splat edges and free surfaces. The compressive residual stress developed near the particle interface could reach 800 MPa for the particles in direct contact with the substrate. Due to higher impact deformation, subsequent impacts increase the compressive stresses developed in the previously deposited particles. The stress state developed across the depth of impacted particles and substrate layer is mainly equibiaxial, with the highest values of stresses occurring in the out-of-plane direction. The simulations show stress wave propagation with a frequency of around 50 MHz and an amplitude of about 100 MPa for Ni particles impacting at 500 m/s and 300 K. Over time, the compressive stress developed near the point of maximum substrate penetration stabilizes to around 380 MPa after approximately 150 ns.
 6. Apart from particle diameter, impact velocity, and ductility, particle morphology strongly influences particle deformation characteristics during the CS process. The non-uniformity of plastic strain and temperature distribution becomes more pronounced for the non-regular shape particles. The deformation of hollow spherical (i.e., $\varepsilon_{pl} > 2$ due to internal holes) causes the greatest impacting particle deformation, which is followed by the other particle types in the following order: $\varepsilon_{pl} 2$ for spherical, $\varepsilon_{pl} 1.8$ for oblate, $\varepsilon_{pl} 1.7$ for angular, $\varepsilon_{pl} 1$ rod-like and $\varepsilon_{pl} 0.8$ for flake-like particles. The spherical particles demonstrate higher flowability and develop more even and wavy-type substrate deformation than the non-spherical ones. Angular particles flatten less and result in a more complex and uneven particle deformation than the other particles. The rod-like and flake-like structures might not stick to the substrate properly as they undergo lower plastic deformation and show more tendency for rigid body motion during the impact period.
 7. The hybrid approach effectively predicts the complex pattern of multiple particle deformation and interactions during the progressive growth of the coating layer, as commonly observed in the microstructure of cold-sprayed coatings. The equivalent plastic strain is significantly higher near interfacial boundaries, with the maximum deformation occurring near the coating-substrate interface. The maximum von Mises stress reaches 750 MPa in the coating layer and 500 MPa in the substrate layer. Stresses near inter-splat interfaces/edges/curved regions are higher than in particle interior or near-surface regions.

In future research, this proposed approach can be used to study the relationship between deposition process parameters, particle grain structure evolution, and coating layer effective properties during the spray process.

Declaration of Competing Interest

The authors declare that they have no known competing financial interests or personal relationships that could have appeared to influence the work reported in this paper.

Acknowledgment

The authors acknowledge the financial support of the Deanship of Scientific Research at King Fahd University of Petroleum and Minerals (KFUPM) and the Interdisciplinary Research Center for Advanced Materials (IRC-AM) through the project EC221002. The author wishes to thank Dr. Khaled S. Al-Athel and Prof. Syed S. Akhtar for their helpful remarks while conducting the research.

Appendix A. Supplementary data

Supplementary data to this article can be found online at <https://doi.org/10.1016/j.jestch.2023.101579>.

References

- [1] H. Assadi, F. Gärtner, T. Stoltenhoff, H. Kreye, Bonding mechanism in cold gas spraying, *Acta Mater.* 51 (2003) 4379–4394.
- [2] H. Wu, X. Xie, S. Liu, X. Xie, R. Huang, C. Verdy, M. Liu, H. Liao, S. Deng, Y. Xie, Bonding behavior of Bi-metal-deposits produced by hybrid cold spray additive manufacturing, *J. Mater. Process. Technol.* 299 (2022), 117375, <https://doi.org/10.1016/j.jmatprotec.2021.117375>.
- [3] A. Vargas-Uscategui, P.C. King, S. Yang, C. Chu, J. Li, Toolpath planning for cold spray additively manufactured titanium walls and corners: effect on geometry and porosity, *J. Mater. Process. Technol.* 298 (2021), 117272, <https://doi.org/10.1016/j.jmatprotec.2021.117272>.
- [4] B. Marzbanrad, E. Toyserkani, H. Jahed, Customization of residual stress induced in cold spray printing, *J. Mater. Process. Technol.* 289 (2021), 116928, <https://doi.org/10.1016/j.jmatprotec.2020.116928>.
- [5] P. Poza, M.Á. Garrido-Maneiro, Cold-sprayed coatings: Microstructure, mechanical properties, and wear behaviour, *Prog. Mater Sci.* 123 (2022), 100839, <https://doi.org/10.1016/j.pmsci.2021.100839>.
- [6] H. Parmar, F. Tucci, P. Carbone, T.S. Sudarshan, Metallisation of polymers and polymer matrix composites by cold spray: state of the art and research perspectives, *Int. Mater. Rev.* 67 (2022) 385–409, <https://doi.org/10.1080/09506608.2021.1954805>.
- [7] Q. Wang, N. Ma, X.-T. Luo, C.-J. Li, Capturing cold-spray bonding features of pure Cu from in situ deformation behavior using a high-accuracy material model, *Surf. Coat. Technol.* 413 (2021), 127087.
- [8] W.Y. Li, K. Yang, S. Yin, X.P. Guo, Numerical analysis of cold spray particles impacting behavior by the eulerian method: a review, *J. Therm. Spray Technol.* 25 (2016) 1441–1460, <https://doi.org/10.1007/s11666-016-0443-3>.
- [9] M. Terrone, A.A. Lordejani, J. Kondas, S. Bagherifard, A numerical framework to design and develop freestanding porous structures through cold spray multi-material deposition, *Surf. Coat. Technol.* 127423 (2021).
- [10] Y.U. Tianyu, C. Mingjun, W.U. Zhuoru, Experimental and numerical study of deposition mechanisms for cold spray additive manufacturing process, *Chin. J. Aeronaut.* (2021).
- [11] B. Gnanasekaran, G.-R. Liu, Y. Fu, G. Wang, W. Niu, T. Lin, A Smoothed Particle Hydrodynamics (SPH) procedure for simulating cold spray process - a study using particles, *Surf. Coat. Technol.* 377 (2019), 124812, <https://doi.org/10.1016/j.surfcoat.2019.07.036>.
- [12] H. Zhou, C. Li, C. Bennett, H. Tanvir, C. Li, Numerical analysis of deformation behavior and interface bonding of Ti6Al4V particle after subsequent impact during cold spraying, *J. Therm. Spray Technol.* 1–14 (2021).
- [13] F. Oviedo, A. Valarezo, Residual stress in high-velocity impact coatings: parametric finite element analysis approach, *J. Therm. Spray Technol.* 29 (2020).
- [14] M. Razavipour, B. Jodoin, Material model for predicting dynamic response of copper and nickel at very high strain rates under cold spray conditions, *J. Therm. Spray Technol.* 30 (2021) 324–343.
- [15] A. Viscusi, M. Bruno, L. Esposito, G. Testa, An experimental/numerical study of bonding mechanism in cold spray technology for metals, *Int. J. Adv. Manuf. Technol.* 110 (2020) 2787–2800, <https://doi.org/10.1007/s00170-020-06060-9>.
- [16] A. Viscusi, Numerical investigations on the rebound phenomena and the bonding mechanisms in cold spray processes, *AIP Conf. Proc.* 1960 (2018), 100017, <https://doi.org/10.1063/1.5034957>.
- [17] X. Song, X.-Z. Jin, W. Zhai, A.-W.-Y. Tan, W. Sun, F. Li, I. Marinescu, E. Liu, Correlation between the macroscopic adhesion strength of cold spray coating and the microscopic single-particle bonding behaviour: Simulation, experiment and prediction, *Appl. Surf. Sci.* 547 (2021), 149165, <https://doi.org/10.1016/j.apsusc.2021.149165>.
- [18] J. Xie, D. Nélias, H. Walter-Le Berre, K. Ogawa, Y. Ichikawa, Simulation of the cold spray particle deposition process, *J. Tribol.* 137 (2015) 41101, <https://doi.org/10.1115/1.4030257>.
- [19] A. Fardan, C.C. Berndt, R. Ahmed, Numerical modelling of particle impact and residual stresses in cold sprayed coatings: a review, *Surf. Coat. Technol.* 409 (2021), 126835, <https://doi.org/10.1016/j.surfcoat.2021.126835>.
- [20] E. Lin, I. Nault, O.C. Ozdemir, V.K. Champagne, A. Nardi, S. Müftü, Thermo-mechanical deformation history and the residual stress distribution in cold spray, *J. Therm. Spray Technol.* 29 (2020) 1424–1436.

- [21] C. Chen, Y. Xie, C. Verdy, R. Huang, H. Liao, Z. Ren, S. Deng, Numerical investigation of transient coating build-up and heat transfer in cold spray, *Surf. Coat. Technol.* 326 (2017) 355–365.
- [22] S. Msolli, Z.-Q. Zhang, J. Guo, S. Narayanaswamy, R.C. Damodara, Z. Zhang, J. Pan, B.H. Tan, Q. Loi, An automated deposition procedure for cold spray additive manufacturing process modeling based on finite element simulation, in: International Conference on Advanced Surface Enhancement, Springer, 2019: pp. 133–143.
- [23] Z. Liu, Finite element analysis of impact and cohesion of cold sprayed particles onto non-planar surfaces, (2021).
- [24] A.A. Abubakar, A.F.M. Arif, S.S. Akhtar, J. Mostaghimi, Splats formation, interaction and residual stress evolution in thermal spray coating using a hybrid computational model, *J. Therm. Spray Technol.* (2019), <https://doi.org/10.1007/s11666-019-00828-6>.
- [25] A.A. Abubakar, A.F.M. Arif, S.S. Akhtar, Evolution of internal cracks and residual stress during deposition of TBC, *Ceram. Int.* 46 (2020) 26731–26753.
- [26] A.A. Abubakar, A.F.M. Arif, A hybrid computational approach for modeling thermal spray deposition, *Surf. Coat. Technol.* (2019), <https://doi.org/10.1016/j.surfcoat.2019.02.010>.
- [27] S. Kumar, M. Kumar, N. Jindal, Overview of cold spray coatings applications and comparisons: a critical review, *World J. Eng.* 17 (2020) 27–51, <https://doi.org/10.1108/WJE-01-2019-0021>.
- [28] S. Rahmati, B. Jodoin, Physically based finite element modeling method to predict metallic bonding in cold spray, *J. Therm. Spray Technol.* 29 (2020) 611–629, <https://doi.org/10.1007/s11666-020-01000-1>.
- [29] H. Assadi, T. Schmidt, H. Richter, J.-O. Kliemann, K. Binder, F. Gärtner, T. Klassen, H. Kreye, On parameter selection in cold spraying, *J. Therm. Spray Technol.* 20 (2011) 1161–1176, <https://doi.org/10.1007/s11666-011-9662-9>.
- [30] R. Nikbakht, H. Assadi, K. Jahani, M. Saadati, B. Jodoin, Cold spray deformation and deposition of blended feedstock powders not necessarily obey the rule of mixture, *Surf. Coat. Technol.* 424 (2021), 127644, <https://doi.org/10.1016/j.surfcoat.2021.127644>.
- [31] ABAQUS, ABAQUS Documentation, Dassault Systèmes. (2016).
- [32] S.T. Oyinbo, T.-C. Jen, Investigation of the process parameters and restitution coefficient of ductile materials during cold gas dynamic spray (CGDS) using finite element analysis, *Addit. Manuf.* 31 (2020), 100986, <https://doi.org/10.1016/j.addma.2019.100986>.
- [33] H. Assadi, I. Irkhin, H. Gutzmann, F. Gärtner, M. Schulze, M. Villa Vidaller, T. Klassen, Determination of plastic constitutive properties of microparticles through single particle compression, *Adv. Powder Technol.* 26 (2015) 1544–1554, <https://doi.org/10.1016/j.appt.2015.08.013>.
- [34] R. Chakrabarty, J. Song, A modified Johnson-Cook material model with strain gradient plasticity consideration for numerical simulation of cold spray process, *Surf. Coat. Technol.* 397 (2020), 125981.
- [35] R. Nikbakht, M. Saadati, H. Assadi, K. Jahani, B. Jodoin, Dynamic microstructure evolution in cold sprayed NiTi composite coatings, *Surf. Coat. Technol.* 421 (2021), 127456, <https://doi.org/10.1016/j.surfcoat.2021.127456>.
- [36] A. Silvello, P.D. Cavaliere, V. Albaladejo, A. Martos, S. Dosta, I.G. Cano, Powder properties and processing conditions affecting cold spray deposition, *Coatings* 10 (2020), <https://doi.org/10.3390/coatings10020091>.
- [37] M. Hassani-Gangaraj, D. Veysset, V.K. Champagne, K.A. Nelson, C.A. Schuh, Adiabatic shear instability is not necessary for adhesion in cold spray, *Acta Mater.* 158 (2018) 430–439, <https://doi.org/10.1016/j.actamat.2018.07.065>.
- [38] C. Sun, X. Zhou, C. Xie, Effect of processing conditions on Al-based amorphous/nanocrystalline coating by cold-spraying, *Surf. Coat. Technol.* 362 (2019) 97–104, <https://doi.org/10.1016/j.surfcoat.2019.01.096>.
- [39] P. Cavaliere, A. Perrone, A. Silvello, Crystallization evolution of cold-sprayed pure Ni coatings, *J. Therm. Spray Technol.* 25 (2016) 1158–1167, <https://doi.org/10.1007/s11666-016-0430-8>.
- [40] A. Viscusi, A. Astarita, R.D. Gatta, F. Rubino, A perspective review on the bonding mechanisms in cold gas dynamic spray, *Surf. Eng.* 35 (2019) 743–771, <https://doi.org/10.1080/02670844.2018.1551768>.
- [41] X. Qiu, N.uL.H. Tariq, L. Qi, J.-R. Tang, X.-Y. Cui, H. Du, J.-Q. Wang, T.-Y. Xiong, Influence of particulate morphology on microstructure and tribological properties of cold sprayed A380/Al2O3 composite coatings, *J. Mater. Sci. Technol.* 44 (2020) 9–18, <https://doi.org/10.1016/j.jmst.2020.01.028>.
- [42] L. Palodhi, B. Das, H. Singh, Effect of particle size and morphology on critical velocity and deformation behavior in cold spraying, *J. Mater. Eng. Perform.* 30 (2021) 8276–8288, <https://doi.org/10.1007/s11665-021-05997-6>.
- [43] J.M. Shockley, S. Descartes, P. Vo, E. Irisson, R.R. Chromik, The influence of Al2O3 particle morphology on the coating formation and dry sliding wear behavior of cold sprayed Al-Al2O3 composites, *Surf. Coat. Technol.* 270 (2015) 324–333, <https://doi.org/10.1016/j.surfcoat.2015.01.057>.
- [44] P.-E. Leger, F. Borit, N. Fabregue, M. Jeandin, M. Ducos, Influence of powder characteristics on the microstructure and bond strength of cold-sprayed aluminum coating, in: ITSC 2016, DVS, Shanghai, China, 2016: p. 6 p. <https://hal-mines-paristech.archives-ouvertes.fr/hal-01337708>.
- [45] W. Wong, P. Vo, E. Irisson, A.N. Ryabinin, J.-G. Legoux, S. Yue, Effect of particle morphology and size distribution on cold-sprayed pure titanium coatings, *J. Therm. Spray Technol.* 22 (2013) 1140–1153.
- [46] K.H. Ko, J.O. Choi, H. Lee, Pretreatment effect of Cu feedstock on cold-sprayed coatings, *J. Mater. Process. Technol.* 214 (2014) 1530–1535, <https://doi.org/10.1016/j.jmatprotec.2014.02.020>.
- [47] H. Assadi, H. Kreye, F. Gärtner, T. Klassen, Cold spraying—a materials perspective, *Acta Mater.* 116 (2016) 382–407.
- [48] D.K. Christoulis, M. Jeandin, E. Irisson, J.-G. Legoux, W. Knapp, Laser-Assisted Cold Spray (LACS), in: D.C. Dumitras (Ed.), IntechOpen, Rijeka, 2012: p. Ch. 5. 10.5772/36104.
- [49] J.A. Lee, M.J. Sagong, J. Jung, E.S. Kim, H.S. Kim, Explainable machine learning for understanding and predicting geometry and defect types in Fe-Ni alloys fabricated by laser metal deposition additive manufacturing, *J. Mater. Res. Technol.* 22 (2023) 413–423, <https://doi.org/10.1016/j.jmrt.2022.11.137>.
- [50] R. Cheng, X. Luo, G. Huang, C.J. Li, Corrosion and wear resistant WC17Co-Tc4 composite coatings with fully dense microstructure enabled by in-situ forging of the large-sized WC17Co particles in cold spray, *J. Mater. Process. Technol.* 296 (2021), 117231, <https://doi.org/10.1016/j.jmatprotec.2021.117231>.